

Chapter 2

“Wet” Chemical Synthesis and Manipulation of Upconversion Nanoparticles

Abstract Development of facile synthesis strategies for high-quality lanthanide-doped upconversion nanoparticles with controlled composition, crystalline phase, shape, and size is crucial in tuning their chemical and optical properties and exploring their potential applications in diverse fields. This chapter focuses primarily on the formation mechanism of the crystallization (including nucleation and growth) for monodisperse nanocrystals and various synthetic procedures for the upconversion nanoparticles. Finally, various optical, chemical, and structural characterizations of upconversion nanoparticles are also summarized.

Keywords Wet chemical synthesis • Upconversion nanoparticles • Upconversion luminescence • Top-down approach • Bottom-up approach • Monodisperse nanocrystals • Optical characterization • Transmission electron microscopy • X-ray photoelectron spectroscopy • X-ray diffraction

2.1 Introduction

Since 1990s, the synthesis of nanocrystals with the sizes ranging from 1 to 100 nm have been intensively pursued, not only for their fundamental scientific interest, but also for their many technological applications. Nanocrystals exhibit very interesting size-dependent electrical, optical, magnetic, chemical, and biological properties that cannot be achieved by their bulk counterparts [1–5]. For many future applications, the synthesis of uniform-sized nanocrystals is of key importance, because the electrical, optical, magnetic, and biological properties of these nanocrystals are strongly dependent on their dimensions. The most popular demonstration of the size-dependent characteristics of nanocrystals are the continuous fluorescent emission from semiconductor nanocrystals (also known as quantum dots) which covers the entire visible spectrum as a function of their size [6, 7]. Monodispersed

Xiaomin Li and Fan Zhang contributed together to this chapter.

magnetic nanocrystals are essential for the next-generation multi-terabit (Tbit/in²) magnetic storage media [8–10]. For the upconversion nanoparticles, the size has a very big influence on its optical and magnetic properties, which makes the upconversion nanoparticles have wide application prospects in optical and MRI bio-imaging [11–13].

There are two different approaches to fabricate nanocrystals: the “top-down” approach, which utilizes physical methods, and the “bottom-up” approach, which employs solution-phase colloidal chemistry (wet chemistry) [10]. The advantage of the physical methods are the production of a large quantity of nanocrystals, whereas the synthesis of uniform-sized nanocrystals and their size control is very difficult to achieve by using the top-down approach. In contrast, wet chemical synthetic methods can be used to synthesize uniform nanocrystals with controlled particle size, although generally only subgram quantities are produced. Furthermore, various-shaped nanocrystals, including nanosphere, nanorods, nanoflowers, nanodisks, etc., can be synthesized by varying the reaction conditions.

Development of facile synthesis strategies for high-quality lanthanide-doped upconversion nanoparticles with controlled composition, crystalline phase, shape, and size is crucial in tuning their chemical and optical properties and exploring their potential applications in diverse fields. With the development of nanotechnology, a variety of methods have been established to synthesize different kinds of upconversion nanoparticles with controlled crystalline phases, sizes, and shapes, (Fig. 2.1) including coprecipitation [14–22], thermal decomposition [23–27], hydro (solvo)thermal synthesis [28–37], sol-gel process [38–41], and combustion synthesis [42], which have been reviewed in many papers [43–54]. This chapter focuses primarily on the formation mechanism of the crystallization (including nucleation and growth) for monodisperse nanocrystals and the various synthetic procedures for the upconversion nanoparticles. Finally, various characterizations for the optical, chemical, and structural properties of upconversion nanoparticles are also summarized.

2.2 Mechanism for the Synthesis of Monodisperse Nanocrystals

The formation processes of monodisperse nanocrystals mainly experience two stages, nucleation and growth. Both of the stage needs to be controlled very carefully. The formation of the monodisperse nanocrystals has been investigated from theory to practice and summarized in some review papers [10]. According to the literature [10], we elaborate the mechanism for the synthesis of monodisperse nanocrystals from three aspects in this section: nucleation, growth, and synthetic techniques for the separation of nucleation and growth.

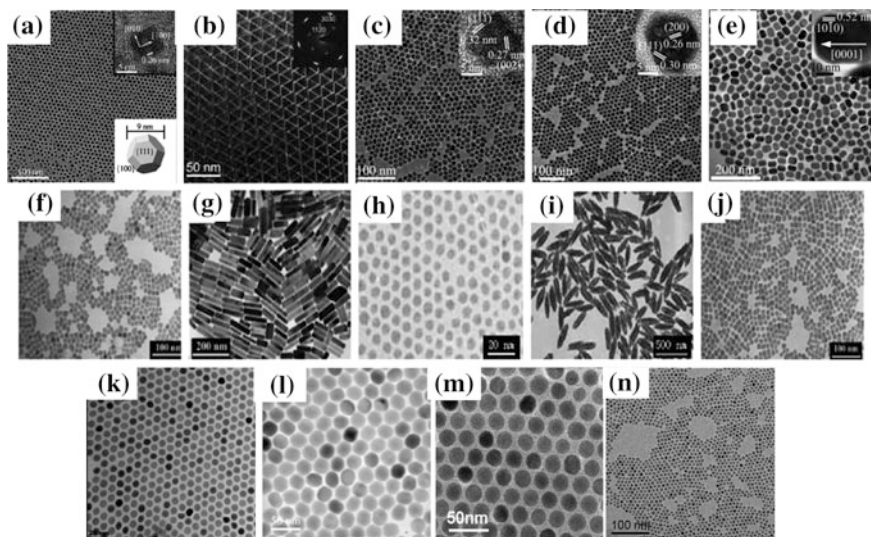


Fig. 2.1 Typical TEM images of lanthanide-doped upconversion nanoparticles. **a** LuOF, **b** LaF₃, **c** α -NaYF₄, **d** NaYbF₄, **e** β -NaEuF₄ synthesized by the thermolysis method, **f** α -NaYF₄:Yb³⁺,Er³⁺, **g** β -NaYF₄:Yb³⁺,Er³⁺, **h** LaF₃, **i** YF₃, **j** α -NaYF₄, synthesized by the hydro(solvo)-thermal method, **k–n** β -NaYF₄ or CaF₂ nanoparticles. **a** Reprinted with the permission from Ref. [55]. Copyright 2007 Wiley-VCH Verlag GmbH & Co. KGaA. **b** Reprinted with the permission from Ref. [26]. Copyright 2005 American Chemical Society. **c–e** Reprinted with the permission from Ref. [24]. Copyright 2006 American Chemical Society. **f, g** Reprinted with the permission from Ref. [45]. Copyright 2011 American Chemical Society. **h–j** Reprinted with the permission from Ref. [37]. Copyright 2005 Nature Publishing Group. **k** Reprinted with the permission from Ref. [56]. Copyright 2012 American Chemical Society. **l** Reprinted with the permission from Ref. [57]. Copyright 2008 Wiley-VCH Verlag GmbH & Co. KGaA. **m** Reprinted with the permission from Ref. [58]. Copyright 2008 American Chemical Society. **n** Reprinted with the permission from Ref. [59]. Copyright 2013 Wiley-VCH Verlag GmbH & Co. KGaA

2.2.1 Nucleation

It is much more difficult to elucidate the mechanism for nanometer-sized particles because of their high surface-to-volume ratios. Although the nucleation and growth processes are strongly correlated, we discuss these two processes separately for the sake of simplicity. The research on the preparation of uniform colloidal particles dates back to the 1940s. LaMer and his colleagues pioneered the concept of “burst nucleation” during the preparation of various oil aerosols and sulfur hydrosols [10, 60, 61]. In this process, many nuclei are generated at the same time, and then these nuclei start to grow without additional nucleation simultaneously. This is the essence of “burst-nucleation” process which makes it possible to control size distribution of particles during growth. Otherwise, if nucleation process occurred throughout the whole particle formation process, the growth history of the particles would differ largely from one another, and consequently, the control of the size distribution would

be very difficult. “Burst nucleation” has been adopted as an important concept in the synthesis of monodispersed nanocrystals. It is well known that to prepare highly uniform nanocrystals, it is necessary to induce a single nucleation event and to prevent additional nucleation during the subsequent growth process. As a synthetic strategy, this method is often referred to as “the separation of nucleation and growth” [10, 60, 61]. LaMer and his colleagues first utilized the homogeneous nucleation process to separate nucleation and growth. In the homogeneous nucleation process, nuclei appear in a homogeneous solution without any seed for heterogeneous nucleation. In this homogeneous nucleation process, there exists a high-energy barrier to nucleation, because the system spontaneously changes from homogeneous to heterogeneous phase. The LaMer plot, as shown in Fig. 2.2a, is very useful for visualizing how the energy barrier works to induce the “burst nucleation” [62, 63]. The concentration of “monomer,” which is the minimum subunit of bulk crystals, constantly increases with time. Note that precipitation does not occur in stage I even under supersaturated conditions ($S > 1$), because the energy barrier for spontaneous homogeneous nucleation is extremely high. In stage II, during the nucleation occurs, the degree of supersaturation is high enough to overcome the energy barrier for nucleation, thus resulting in the formation and accumulation of stable nuclei. Since the rate of monomer consumption resulted from the nucleation and growth processes exceeds the rate of monomer supply, the monomer concentration decreases until it reaches the level at which the net nucleation rate (the number of nuclei formed per unit time) is zero. Below this level, the system enters the growth stage (stage III), in which nucleation is effectively stopped and the particles keep growing as long as the solution is supersaturated. Once monomer concentration is sufficiently depleted, growth can proceed by Ostwald ripening (stage IV). Here, sacrificial dissolution of smaller (higher-surface-energy) particles results in growth of larger particles and, thereby, fewer particles in the system.

According to literature [10, 61, 64–67], the energy barrier to the homogeneous nucleation is interpreted thermodynamically as follows: The Gibbs free energy of

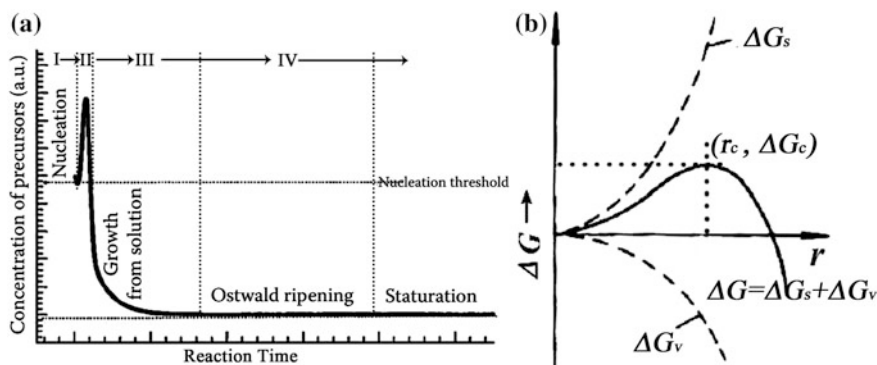


Fig. 2.2 **a** Schematic depicting the four stages of the preparation of monodisperse nanocrystals in the framework of the LaMer model. **b** Illustration of the surface free energy (ΔG_s), bulk free energy (ΔG_v), and overall free energy (ΔG) as a function of the growth particle size r

formation of spherical crystals with radius r from the solution with supersaturation S is given in Eq. (2.1), in which σ is the surface free energy per unit area and ΔG_v is the free energy change between the monomers in the solution and unit volume of bulk crystal, V_m is the molar volume of bulk crystal.

$$\Delta G = 4\pi r^2 \sigma + \frac{4}{3} \pi r^3 \Delta G_v = 4\pi r^2 \sigma + \frac{4}{3} \pi r^3 (-RT \ln S) / V_m \quad (2.1)$$

σ is always positive, and ΔG_v is negative as long as the solution is supersaturated. Consequently, a plot of ΔG versus r has a maximum. The value of r at which ΔG is maximum is called the critical radius r_c ; this is the minimum radius of a nucleus that can grow spontaneously in the supersaturated solution. Setting $d\Delta G/dr = 0$ allows determination of r_c .

$$r_c = \frac{-2\sigma}{\Delta G_v} = \frac{2\sigma V_m}{RT \ln S} \quad (2.2)$$

Equation (2.2) imposes the first necessary condition for supersaturation with homogeneous nucleation. Because r_c is the minimum radius that will persist and not dissolve away in solution, S should be sufficiently high for r_c to be smaller than the size of the crystal embryos that form the nuclei for the homogeneous nucleation process [64, 65]. Although little is known about the identity of the crystal embryos, their sizes might be less than 1 nm, which is comparable to the size of inorganic molecular clusters. Substituting Eq. (2.2) into Eq. (2.1) gives the critical free energy ΔG_c (Eq. 2.3), which is the free energy necessary to form a stable nucleus.

$$\Delta G_c = \frac{16\pi\sigma^3}{3(\Delta G_v)^2} = \frac{16\pi\sigma^3 V_m^2}{3(RT \ln S)^2} \quad (2.3)$$

If the rate of increase of the number of particles N is defined as the rate of nucleation (k_B is the Boltzmann constant), it can be written in the Arrhenius form in terms of ΔG_c (Eq. 2.4).

$$\frac{dN}{dt} = A \exp \left[-\frac{\Delta G_c}{k_B T} \right] = A \exp \left[\frac{16\pi\sigma^3 V_m^2}{3k_B^3 T^3 N_A^2 (\ln S)^2} \right] \quad (2.4)$$

At this point, it should be noted that, in contrast to the simple LaMer plot, it is hard to define exactly the critical supersaturation level at which nucleation begins, because nucleation and redissolution can happen at any concentration, as a result of the energy fluctuation in the solution. In fact, the nucleus can still form even in unsaturated solution, and the particles formed could re-dissolve unless they are stable enough to resist the free energy fluctuation of their surroundings. However, from the practical point of view, it is reasonable to establish the critical supersaturation level (S_c) at which stable nuclei form in an appreciable number per unit time

and start to accumulate. To see how this condition affects S , we rewrite Eq. (2.4) so as to express S in terms of N' ($=dN/dt$) (Eq. 2.5).

$$\ln S = \sqrt{\frac{16\pi\sigma^3 V_m^2}{3k^3 T^3 \ln(A/N')}} \quad (2.5)$$

This equation shows another necessary condition pertaining to the degree of supersaturation: To start the accumulation and the growth of the nuclei, the nucleation rate should be high enough to equilibrate or to surpass the redissolution rate of the particles. Taken together, S_c is the point at which the nucleation rate is so high that the number of nuclei increases even while smaller nuclei dissolve away.

However, the thermodynamic model discussed so far has some limitations with respect to nanocrystals. Whereas it is generally assumed that σ and ΔG_v are constant, these two values are strongly size-dependent for nanometer-sized particles [66]. As the particle size decreases, the ratio of surface atoms to the bulk atoms dramatically increases. As a result, there is a strong driving force, especially for nanocrystals with a size of few nanometers, to minimize the surface free energy by reconstructing the surface structure or changing the crystal structure (e.g., through phase transitions [67] or lattice contraction [61, 68]).

2.2.2 *Synthetic Techniques for the Separation of Nucleation and Growth*

Both homogeneous and heterogeneous nucleation processes have been utilized to synthesize monodisperse nanocrystals by separating nucleation and growth. The seed-mediated growth method is the most apparent case for the separation of nucleation and growth, wherein nucleation is physically separated from growth by using preformed nanocrystals as seed nuclei. This method utilizes heterogeneous nucleation to suppress the formation of additional nuclei by homogeneous nucleation [69–72]. In this method, preformed nuclei are introduced into the reaction solution and then the monomers are supplied to precipitate on the surface of the existing nuclei. The monomer concentration is kept low during growth to suppress homogeneous nucleation. Seed-mediated growth is further divided into two categories: the synthesis of homogeneous particles [69, 72] and the production of heterogeneous structures, such as core/shell structures [70, 71]. There have been several reports on the fine size control of nanocrystals by separating nucleation and growth by the seed-mediated growth process [71, 72]. However, the seed particles need to be uniform to produce monodisperse nanocrystals.

There are two techniques that utilize homogeneous nucleation to synthesize monodisperse nanocrystals in the organic solutions: “hot-injection” [73–75] and “heating-up” methods [76–79]. The “hot-injection” technique was introduced by Bawendi and coworkers in their report on the synthesis of cadmium chalcogenide

nanocrystals [68]. This technique produces high degree of supersaturation by the rapid injection of excess precursor into a hot surfactant solution, resulting in burst nucleation by relieving the excess free energy of the supersaturation. During the nucleation process, the monomer concentration in the solution sharply decreases and thus nucleation rate slows down. This “hot-injection” method has been widely used to synthesize nanocrystals of metal chalcogenides [68, 73], transition metals [74], noble metals [75], and upconversion nanoparticles [80]. The heating-up method is a batch process in which the precursors, reagents, and solvent are mixed at a low temperature and heated up to a certain temperature to initiate the crystallization reaction. The heating-up method is particularly advantageous for large-scale production, because of its simplicity. Although this synthetic procedure is very simple, the size uniformity of the nanoparticles yielded by the heating-up method is often comparable to the best results obtained from the “hot-injection” method [76, 77]. Characterizing the burst-nucleation process is challenge. Characteristic for this process is that there is a point of time at which the number of particles stops increasing and the particle concentration reaches a maximum. After this point, the reaction system enters the growth stage and number of particles either remains constant or decrease. According to LaMer’s model, the end of the nucleation stage is closely related to the decrease of the monomer concentration. Consequently, to prove the “burst-nucleation” model experimentally, both the particle concentration and the monomer concentration should be traced simultaneously.

2.2.3 Growth

In the previous section, we mentioned that the separation of nucleation and growth makes it possible to control the size distribution of an ensemble of particles. In this section, the significance of growth without additional nucleation as a necessary condition for a narrow size distribution of the ensemble of particles will be shown [10].

The first theoretical study on the narrowing of the size distribution during the growth process was performed by Reiss [81]. In his model, known as the “growth by diffusion” model, the growth rate of spherical particles depends solely on the flux of the monomers supplied to the particles (J). In this case, the relationship between the monomer flux and the growth rate dr/dt is given by Eq. (2.6).

$$J = \frac{4\pi r^2}{V_m} \frac{dr}{dt} \quad (2.6)$$

If the average distance between the particles is large enough, then the diffusion layer formed at the periphery of each particle is undisturbed. Consequently, it is possible to treat each growing particle independently. For a single spherical particle in a homogeneous medium, there is concentration gradient around a particle

with spherical symmetry. Fick’s law (Eq. 2.7) gives the flux J of monomers diffusing through the surface of a sphere enclosing the particle (D is the diffusion coefficient, C is the concentration, and $x (\geq r)$ is the distance from the center of the particle).

$$J = 4\pi x^2 D \frac{dC}{dx} \quad (2.7)$$

If J is assumed to be constant for x , the integration of $C(x)$ from r to $r + \delta$ with respect to x gives Eq. (2.8).

$$J = 4\pi D \frac{r(r + \delta)}{\delta} [C_{(r+\delta)} - C_s] \quad (2.8)$$

$C_s (=C_r)$ is the concentration at the surface of the particle. For sufficiently large values of δ ($r \ll \delta$), Eq. (2.8) is reduced to Eq. (2.9), in which C_{bulk} is the concentration of the bulk solution.

$$J = 4\pi r D (C_{\text{bulk}} - C_s) \quad (2.9)$$

Equation (2.10) follows from Eqs. (2.6) and (2.9).

$$\frac{dr}{dt} = \frac{V_m D}{r} (C_{\text{bulk}} - C_s) \quad (2.10)$$

If C_s and C_{bulk} are constant for all particles, the growth rate of a particle is inversely proportional to its radius. This result can be understood intuitively as follows: The number of monomers diffused onto the surface of a particle increases in proportion to the square of its radius, whereas the volume of a particle consisting of the monomers increases in proportion to the third power of its radius. Thus, the growth rate of a particle is decreased as the radius increases. With this result, it can be shown that for an ensemble of spherical particles, the variation of the radius distribution σ^2 is decreased during growth. From Eq. (2.10), the value of σ^2 can be obtained as Eq. (2.11), in which r and $(1/r)$ are the mean values of r and $1/r$, respectively.

$$\frac{d\sigma^2}{dt} = 2V_m D (C_{\text{bulk}} - C_s) \left[1 - \bar{r} \overline{\left(\frac{1}{r} \right)} \right] \quad (2.11)$$

Because the arithmetic mean differs from the harmonic mean, $(1/r)$ is always greater than $1/\bar{r}$. Thus, for $C_{\text{bulk}} > C_s$, the right-hand side of Eq. (2.11) is always negative. In other words, the variance of the size distribution of an ensemble of particles always decreases regardless of the initial size distribution as long as all of the particles are growing and no additional nucleation occurs. This is the self-regulating mechanism of the size distribution during the growth process and is often referred to as the “focusing” effect [63].

However, the model described by Reiss is an oversimplification because it does not consider the reaction kinetics of crystal growth and its dependence on the particle size. As a result, the strong counter effect for the “focusing” mechanism is missing. During the growth process, there are two reactions acting in opposition to each other, namely, precipitation and dissolution (Eq. 2.12).



M^s and M^c refer to monomers in solution and in the crystal, k_p and k_d are the reaction rate constants for precipitation and dissolution, respectively. It is assumed that the precipitation is the first-order reaction with respect to C_s and that the dissolution rate is independent of C_s . Then, at equilibrium $k_p C_{s,eq} = k_d$, which can be rewritten to give the surface concentration $C_{s,eq}$ (Eq. 2.13)

$$C_{s,eq} = \frac{k_d}{k_p} \quad (2.13)$$

The change in chemical potential $\mu(r)$ of a spherical crystal with radius r with respect to that μ^o of the bulk crystal arises from the surface free energy of area (A) (Eq. 2.14).

$$\Delta\mu = \mu(r) - \mu^o = \gamma \frac{dA}{dn} \quad (2.14)$$

Because $dA = 8\pi r dr$ and $dn = 4\pi r^2 dr/V_m$, Eq. (2.14) can be rewritten as the Gibbs–Thomson relation Eq. (2.15).

$$\Delta\mu = \frac{2\gamma V_m}{r} \quad (2.15)$$

The activated complex theory is adopted to assess the effect of the chemical potential change of a crystal on the precipitation and dissolution reactions. The variation of k_p and k_d with $\Delta\mu$ is given as Eqs. (2.16) and (2.17).

$$k_p = k_p^o \exp\left[-\alpha \frac{\Delta\mu}{RT}\right] = k_p^o \exp\left[-\alpha \frac{2\gamma V_m}{rRT}\right] \quad (2.16)$$

$$k_d = k_d^o \exp\left[(1 - \alpha) \frac{\Delta\mu}{RT}\right] = k_d^o \exp\left[(1 - \alpha) \frac{2\gamma V_m}{rRT}\right] \quad (2.17)$$

In these equations, α is the transfer coefficient and k^o is the rate constant for the bulk crystal ($r = \infty$) [82]. Qualitatively, Eqs. (2.16) and (2.17) reveal that the smaller the radius of a particle is, the harder it is to grow but the easier it is to dissolve, because of its higher chemical potential. This is the effect in contrast to the “focusing” mechanism, in which smaller crystals grow faster. To combine this effect with the

model of Reiss, the assumption that C_s is constant for all particles should be modified. The fluxes of the monomers toward the surface of a particle by precipitation and dissolution (J_p and J_d , respectively) for a particle with radius r are given by Eqs. (2.18) and (2.19)

$$J_p = 4\pi r^2 k_p^o C_s \exp\left[-\alpha \frac{2\gamma V_m}{rRT}\right] \quad (2.18)$$

$$J_d = -4\pi r^2 k_d^o \exp\left[(1 - \alpha) \frac{2\gamma V_m}{rRT}\right] \quad (2.19)$$

The net flux J , then, is given by Eq. (2.20), and the equation for C_s (Eq. 2.21) is obtained by equating the expressions for J in Eqs. (2.9) and (2.20)

$$J = J_p + J_d = 4\pi r^2 k_p^o C_s \exp\left[-\alpha \frac{2\gamma V_m}{rRT}\right] - 4\pi r^2 k_d^o \exp\left[(1 - \alpha) \frac{2\gamma V_m}{rRT}\right] \quad (2.20)$$

$$C_s = \frac{k_d^o r \exp\left[(1 - \alpha) \frac{2\gamma V_m}{rRT}\right] + DC_{\text{bulk}}}{k_p^o \exp\left[-\alpha \frac{2\gamma V_m}{rRT}\right] + D} \quad (2.21)$$

Substituting this result into Eq. (2.10) and using Eq. (2.13) leads to Eq. (2.22). $C_{s,\text{eq}}^o$ is the equilibrium surface concentration of the bulk crystal ($r = \infty$), and S is the degree of supersaturation, which is defined as $S = C_{\text{bulk}}/C_{s,\text{eq}}^o$. This result can be rewritten in simplified form as Eq. (2.23) [82].

$$\frac{dr}{dt} = V_m DC_{s,\text{eq}}^o \left[\frac{S - \exp\left[\frac{2\gamma V_m}{rRT}\right]}{r + \frac{D}{k_p^o} \exp\left[\alpha \frac{2\gamma V_m}{rRT}\right]} \right] \quad (2.22)$$

$$\frac{dr^*}{d\tau} = \frac{S - \exp(1/r^*)}{r^* + K \exp(\frac{2}{r^*})} \quad (2.23)$$

The variables and parameters in Eq. (2.23) can be normalized to dimensionless forms (Eqs. 2.24–2.26)

$$r^* = \frac{RT}{2\gamma V_m} r \quad (2.24)$$

$$\tau = \frac{R^2 T^2 DC_{s,\text{eq}}^o}{4\gamma^2 V_m} t \quad (2.25)$$

$$K = \frac{RT}{2\gamma V_m} \frac{D}{k_p^o} \quad (2.26)$$

Equation (2.23) is a modified version of Eq. (2.10) after both the mass transport and the reaction kinetics are considered. The growth rate of a single particle for various values of K and S are calculated from Eq. (2.23) and plotted in Fig. 2.3a, b.

In Reiss' simple model, the "focusing" effect is derived by considering only mass-transport processes. However, the opposite effect comes from a kinetic process related to the Gibbs–Thomson effect. Figure 2.3a, b shows how these two effects compete with each other for the growth of an individual particle. A typical plot of growth rate for small values of K ($\ll 1$) and large values of S ($\gg 1$) has a maximum at $r^* = r_{\max}^*$. For $r^* > r_{\max}^*$, the size dependence of the crystal chemical

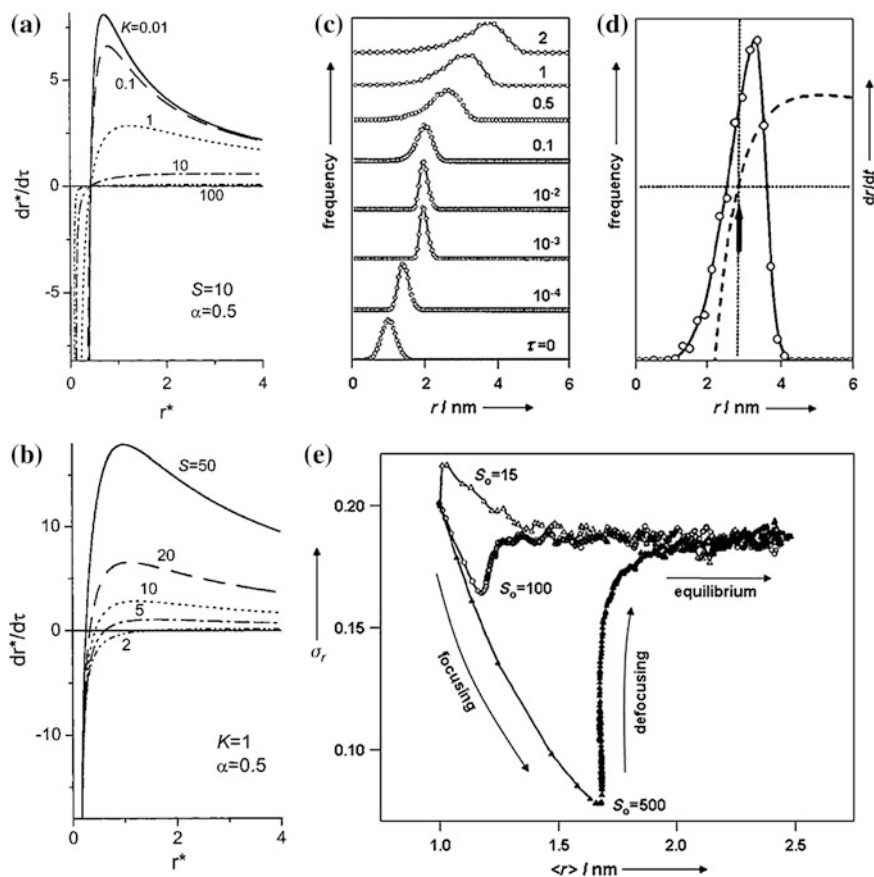


Fig. 2.3 Growth rate as a function of radius calculated from Eq. (2.23) for various values of K (a) and S (b). $\alpha = 0.5$, $S = 10$ in (a), and $K = 1$ in (b). c Time evolution of the size distribution of the ensemble of particles. d The size distribution of particles (open circles and solid line) and the growth rate as a function of radius (dashed line) in the later period of the reaction. The arrow indicates the position of r_{zero} . e Relative standard deviation versus mean radius for different initial levels of supersaturation. a–c, e Reprinted with the permission from Ref. [82]. Copyright 2001 American Chemical Society. d Reprinted with the permission from Ref. [83]. Copyright 2002 American Chemical Society

potential is relatively small such that the variation of the growth rate with r^* mainly depends on mass-transport effects rather than on kinetic effects. Consequently, the slope of the graph is negative and a narrowing of the size distribution occurs in this region (the “focusing” region). In contrast, for $0 < r^* < r_{\max}^*$, the situation is reversed. In this region, the crystal chemical potential is highly sensitive to the particle size. As r^* decreases, a particle becomes more unstable and the dissolution rate increases so fast that it dominates the net growth rate. As a result, larger particles have a higher growth rate and the slope of the graph is positive (the “defocusing” region). At $r^* = r_{\text{zero}}^*$, the growth rate is zero, and the rates of precipitation and dissolution are balanced. The value of r_{zero} can be obtained from Eqs. (2.23) and (2.24) (Eq. 2.27).

$$r_{\text{zero}} = \frac{2\gamma V_m}{RT r_{\text{zero}}^*} = \frac{2\gamma V_m}{RT \ln S} \quad (2.27)$$

It is notable that this value is equal to r_c , which is evaluated by Eq. (2.2) from the nucleation model. From Fig. 2.3a, b, the factors affecting the evolution of the size distribution can also be deduced. In Eq. (2.27), K represents the ratio of the rate of diffusion to the rate of the precipitation reaction. If the value of K is very small, the overall growth reaction rate is controlled by the diffusion rate, that is, the rate of mass transfer. This condition is called diffusion-controlled growth and is similar to the growth condition in Reiss’ model. Consequently, the smaller the value of K is, the more effective the narrowing of the size distribution becomes. However, if the value of K is very large, the growth rate is mainly determined by the reaction rate. This condition is called reaction-controlled growth and the “focusing” effect is weakened under this condition. This trend is depicted in Fig. 2.3a, which shows a steep negative slope for small values of K . An increase in the value of S always results in the enhancement of the growth rate according to Eq. (2.23). However, the increment of the growth rate with S is decreased by a factor of $1/[r^* + K \exp(a/r^*)]$ and thus is larger for smaller particles. In short, both the increase of S and the decrease of K enhance the “focusing” mechanism.

For an ensemble of particles, it is very difficult to trace the time evolution of the size distribution, mainly because C_{bulk} is not a constant but rather a function of the size of all the particles in the ensemble. Furthermore, the growth rates also depend on C_{bulk} . This mutual dependence makes it very difficult, if not impossible, to derive analytically the time evolution of the size distribution of the particles from Eq. (2.23).

Talpin et al. [82] presented another approach to solve this problem. They performed a numerical simulation of the time evolution of the particle size in an ensemble by using the Monte Carlo method (Fig. 2.3c–e). They used Eq. (2.23) to calculate the growth rate for an individual particle. The initial size distributions of the ensembles of particles were set to normal distributions with various relative standard deviations and a mean value of $r_0 = 1$ nm. With these given ensembles of particles, simulations of the growth process were started with an initial supersaturation S_0 . Figure 2.3c shows the time evolution of the size distribution of the

particle ensemble. The initial reaction solution is highly supersaturated and the growth reaction operates under the diffusion-controlled condition. Two periods in the growth process can be distinguished in this figure. Initially ($0 < \tau < 10^{-2}$), the mean radius increases rapidly and the size distribution becomes narrower. In this period, the supersaturation is so high that r_{zero}^* is far below the mean radius \bar{r}^* , and consequently, all of the particles are in the “focusing” region. In the second stage ($10^{-2} < \tau$), the growth rate declines sharply and the size distribution broadens. In this period, the supersaturation is low because of the rapid consumption of the monomer during the early period. As a result, the value of r_{zero}^* becomes comparable to that of \bar{r}^* and many of the particles in the ensemble fall into the “defocusing” region (Fig. 2.3d). Figure 2.3e depicts the relationship between the mean radius and the relative standard deviation of the size distribution for different initial supersaturations: A high initial supersaturation causes the “focusing” period to be maintained for a large mean radius, resulting in a low relative standard deviation at the end of the “focusing” period. Figure 2.3e also shows that the “defocusing” period leads to a similar equilibrium relative standard deviation regardless of the initial supersaturation. In the “defocusing” and equilibrium periods in which r_{zero} lies near \bar{r}^* , Ostwald ripening occurs. In this process, smaller particles dissolve and larger particles grow by receiving the monomers from the dissolving particles (This process was described in the previous section as an explanation for the decrease of the particle concentration during the growth stage). When the Ostwald-ripening process is under pseudoequilibrium state, the dissolving rate and reprecipitation rate of the monomers are balanced and the degree of supersaturation declines very slowly. Generally, the Ostwald ripening broadens the standard deviation of the particle size distribution. At the same time, the mean size of the particle ensemble is also increased. As a result, the relative standard deviation (the standard deviation divided by the mean value) converges to a certain value as the reaction system enters the pseudoequilibrium state. According to the simulation results by Talapin et al. [82], the relative standard deviation in the equilibrium period is almost independent of the initial size distribution but is lowered when the surface free energy is high.

The theoretical works discussed so far explain the behavior of the size distribution during the growth process when there is no additional nucleation. The theoretical studies and simulations of Talapin et al. [81–83] reveal two underlying mechanisms for the control of the size distribution: (1) The “focusing” effect is a kinetically driven process that actively reduces the variance of the particle size distribution during the growth process. It works when the growth process is diffusion controlled and the degree of supersaturation is high. (2) Ostwald ripening occurs when the supersaturation is low. Experimental evidence for the “focusing effect” was provided by Alivisatos and coworkers, who reported that the size distribution of the semiconductor nanocrystals is strongly correlated with the degree of supersaturation [63]. They synthesized CdSe nanoparticles by the hot-injection method and traced the time evolution of the size and the size distribution of the nanocrystals by using photoluminescence (PL) spectroscopy. They observed that

a fast increase of the mean particle size and a narrowing of the size distribution occurred simultaneously during the initial period of the growth process. In the later period, the growth rate decreased and the size distribution gradually broadened. The injection of additional monomers during this period resulted in the same effect as that observed during the initial period. This result confirms the relationship between the supersaturation level and the size “focusing” by growth and, consequently, supports the “focusing” mechanism.

2.3 Synthesis Routes for the Upconversion Nanoparticles

Based on the above-mentioned formation mechanism of the monodisperse nanocrystals, a range of synthetic approaches such as thermal decomposition, hydro (solvo)thermal synthesis, Ostwald-ripening method, sol-gel processing, coprecipitation method, as well as ionic liquid-based synthesis have been investigated to synthesize monodisperse high-quality lanthanide-doped upconversion nanoparticles. This section mainly focuses on thermolysis, hydro(solvo)thermal synthesis, etc., which are the most widely used methods, as they can offer precise control over the phase, shape, size, and stoichiometric composition of the core-only and/or the core/shell upconversion nanoparticles. Table 2.1 is a summary of upconversion nanoparticles of varied host materials prepared by these methods.

2.3.1 Thermolysis Strategy

The thermolysis strategy generally employs organometallic compounds as precursors, which decompose in a high boiling point organic solvent with the assistance of surfactants at an elevated temperature. The commonly used precursors are metallic trifluoroacetate salts or oleatum; the solvent can be 1-octadecene (ODE), paraffin oil, etc.; the surfactants can be oleic acid (OA), oleylamine (OM), or trioctylphosphine oxide (TOPO), which typically contain a functional capping group to coordinate the metallic elements and the long hydrocarbon chain to prevent nanoparticle aggregation. It is important to note that the rapid decomposition of metallic trifluoroacetate creates a burst of nucleation, which is essential for producing monodispersed nanoparticles. By carefully tailoring the experimental variables, such as the nature of solvents, concentration of metal precursors, reaction temperature, and time, high-quality upconversion nanoparticles with a narrow size distribution, good crystallinity, and exceptional optical properties can be readily obtained from the thermolysis process. The drawback of the thermolysis strategy is that the toxic by-products of fluorinated and oxyfluorinated carbon species mandate a carefully exercised synthetic procedure. Due to the hydrophobic properties of the ligands, the other disadvantage of the thermolysis method is the indispensably post-surface hydrophilic modification, especially for the bio-applications.

Table 2.1 Typical upconversion host materials and their synthetic strategies

Synthetic method	Solvent	Hosts	Morphology	Size (nm)	References
Thermolysis	OA, ODE	NaYbF ₄	Sphere, polyhedron, sphere, polyhedron	15–30	[24, 84, 85]
		NaGdF ₄		6–15	[24, 86–88]
		NaYF ₄	Hexahedron, sphere, nanorod, nanocubic, nanoplate, nanoprism	10–100	[23, 24, 89–91]
		LiYF ₄	Nanospindle, hexahedron, sphere, nanorod, nanocubic, sphere, nanocubic	20–100	[92–94]
		NaLnF ₄ (Ln = Nd, Sm, Eu, Tb, Dy, Ho, Er, Tm, Lu)		10–150	[24]
		CeO ₂		5–80	[95, 96]
		LaF ₃	Nanozigzag, nanoplate	10–50	[26, 55]
		YF ₃	Sphere, parallelogram	3–10	[55, 97]
		MF ₂ (M = Mg, Ca, Sr)	Nanoneedle, nanocubic	30–100	[98]
		LnF ₃ (Ln = Ce, Pr, Nd, Sm, Eu, Gd, Tb, Dy, Ho, Tm, Yb, Lu); LnOF (Ln = Er, Tm, Yb, Lu, Tb, Dy, Ho, Y)	Nanoplate, sphere, nanozigzag, truncatedoctahedron, nanorods, nanopolyhedra	5–20	[55]
		NaScF ₄	Nanocubic, nanohexahedron	20–30	[99]
	OAM	NaYF ₄	Sphere	10–50	[100]
		LaOF	Sphere	3–10	[55, 101]
		GdOF	Sphere, nanorods	2–10	[101]

(continued)

Table 2.1 (continued)

Synthetic method	Solvent	Hosts	Morphology	Size (nm)	References
	OAM, ODE	LnOCl	Nanorod, nanoplate	3–200	[102]
	OA, OAM	NaYF ₄	Sphere	5–20	[103, 104]
		EuOF	Nanowire, polyhedron	3–5	[55]
		GdOF	Nanorod, polyhedron	3–5	[55, 101]
		LnF ₃ (Ln = Dy, Ho, Er)	Triangular, nanoplate, nanozigzag,	2–20	[55]
		LnOF (Ln = Ce, Pr, Nd, Sm, Tb, Dy, Ho, Y)	Nanoquadrilateral, nanopolygonal, Nanorod	2–20	[55]
		Ln ₂ O ₃ (Ln = La, Pr, Nd, Sm, Eu, Y)	Nanodisk, nanoplate, nanocubic	5–20	[105]
		LnPO ₄ (Ln = Ln, Eu, Tb, Y, Ho)	Nanopolyhedron, nanowire, nanoplate, nanorod, nanowormlike wire, nanoquasirod	3–200	[106]
	OA, OAM, ODE	Eu ₂ O ₂ S	Nanoplate, nanorod	10–15	[107]
		La ₂ O ₂ S	Nanoplate	25–30	[108]
		Gd ₂ O ₃	Nanoplate, nanodisk	8–10	[105, 106]
		Ln ₂ O ₃ (Ln = Tb, Dy, Ho, Er, Tm, Yb, Lu, Y)	Nanoplate, nanodisk	5–20	[105]
		NaLnS ₂ (Ln = La, Sm, Tb, Ce)	Nanoplate, nanocubic	10–200	[109]
		NaLnF ₄ (Ln = Pr, Nd, Sm, Eu, Tb, Dy, Ho, Er, Tm, Yb, Lu, Gd)	Nanopolyhedron, nanorod, hexahedron	5–500	[24]
		NaYF ₄	Nanopolyhedron, nanorod, hexahedron, nanocage	10–200	[24, 110]
		LiYF ₄	Sphere	10–12	[111]
OA, TOPO		Y ₂ O ₃	Nanodisk	4–6	[112]
		NaYF ₄	Nanorod, sphere, nanoplate, nanocubic	9–150	[113–115]
					(continued)

Table 2.1 (continued)

Synthetic method	Solvent	Hosts	Morphology	Size (nm)	References
Hydrothermal		NaYF ₄	Sphere, nanoplate, nanocubic	5–500	[30, 36, 37, 58, 116–119]
		Er ₂ O ₃	Sphere, nanorod	3–3,000	[120]
		BaYF ₅	Sphere, microcubic	10–1,000	[121]
		CeO ₂	Sphere, microcubic	5–1,5	[122]
		SrF ₂	Sphere	5–6	[123]
		CaF ₂	Nanocubic	5–8	[31]
		LaF ₃	Sphere, nanoplate	5–65	[116, 117, 124]
		GdF ₃	Sphere	10–20	[116]
		NaYbF ₄	Sphere, polyhedron	5–25	[30, 116]
		CeF ₃	Sphere, nanocubic	5–8	[125, 126]
		NaCeF ₄	Nanowire, nanorod	100–1,000	[125]
		Na ₃ MF ₇ (M = Zr, Hf)	Nanocubic	6–8	[127]
		BaY ₂ F ₈	Nanobelt	75 × 1,000	[128]
		YbPO ₄ , LuPO ₄	Sphere	5–10	[21]
		NaLnF ₄ (Ln = Pr, Nd, Sm, Eu, Gd, Dy, Ho, Er, Tm, Tb)	Polyhedron, nanotube, nanodisk, nanorod	3–800	[30]
		KYF ₄	Sphere	20–50	[129]
		NaLuF ₄	Nanoplate	15–150	[30, 130]

The thermolysis strategy can be divided into three groups according to the solvents (i.e., surface ligands) used in the synthesis.

Thermolysis in oleic acid-based mixed solvents: This thermolysis method was first developed by the Yan group to synthesize highly monodispersed LaF_3 nanoparticles [26]. The approach was later extended as a common route to synthesize high-quality cubic lanthanide-doped NaYF_4 upconversion nanoparticles [23–25]. For example, Capobianco and coworkers reported the synthesis of cubic NaYF_4 nanoparticles codoped with $\text{Yb}^{3+}/\text{Er}^{3+}$ or $\text{Yb}^{3+}/\text{Tm}^{3+}$ via thermal decomposition of metal trifluoroacetate precursors in the presence of OA and ODE [25]. In their studies, the non-coordinating ODE was used as the primary solvent due to its high boiling point. OA was chosen not only as a solvent but also as a passivating ligand that prevents the nanoparticles from agglomeration. The same approach was further refined by Capobianco et al. to synthesize cubic upconversion NaYF_4 nanoparticles with a remarkably narrow size distribution without the need for size-selective fractionation [23]. The approach was based on temporal separation of nucleation and crystal growth by slow addition of the precursors to the solution and subsequent manipulation of the temperature. Another outstanding demonstration was reported by Murray and coworkers who prepared highly uniform hexagonal $\text{NaYF}_4:\text{Yb}^{3+}/\text{Er}^{3+}$ nanoparticles with controlled sizes and morphologies (spheres, nanorods, and hexagonal prisms) by using the same synthetic strategy [90]. These as-prepared nanoparticles can be easily assembled into large-area super-lattices under appropriate conditions. The decomposition method has also been extended to synthesize other RE fluorides, oxides, and oxyfluorides such as LiREF_4 [92–94], $\text{KRE}_3\text{F}_{10}$ [131], NaScF_4 [99], YF_3 [55, 97], MF_2 ($\text{M} = \text{Mg}, \text{Ca}, \text{and Sr}$) [98], BaREF_5 [132], CeO_2 [95, 96], and LnOF ($\text{Ln} = \text{Er}, \text{Tm}, \text{Yb}, \text{Lu}, \text{Tb}, \text{Dy}, \text{Ho}, \text{Y}$) [55].

Thermolysis in oleylamine (OAM)-based mixed solvents: Yan and coworker also presented systematic and general synthesis of high-quality Ln_2O_3 ($\text{Ln} = \text{Tb}, \text{Dy}, \text{Ho}, \text{Er}, \text{Tm}, \text{Yb}, \text{Lu}, \text{Y}$) [105] and LnOF ($\text{Ln} = \text{Ce}, \text{Pr}, \text{Nd}, \text{Sm}, \text{Tb}, \text{Dy}, \text{Ho}, \text{Y}$) nanoparticles with diverse shapes in OA/OAM, as well as NaYF_4 and NaLnF_4 ($\text{Ln} = \text{Pr}, \text{Nd}, \text{Sm}, \text{Eu}, \text{Tb}, \text{Dy}, \text{Ho}, \text{Er}, \text{Tm}, \text{Yb}, \text{Lu}, \text{Gd}$) nanoparticles in OA/OAM/ODE solvents [12, 24, 55, 98, 101, 105, 133]. They refined this technique to the general synthesis of a whole range of rare earth fluorides, rare earth oxide, and rare earth oxyfluoride nanoparticles with multiform crystal phases and morphologies by manipulating the ratio of precursors, solvent composition, reaction temperature, and time. For the synthesis of fluoride nanoparticles, it was found that the combined use of coordinating ligands of the OA and the OAM could produce sub-10-nm cubic lanthanide-doped NaYF_4 nanoparticles, which was generally much smaller than the ones produced using OA as the ligand and the ODE as a high-boiling solvent [104]. It is interesting to note that ~ 10 nm monodisperse hexagonal phase $\text{NaYF}_4:\text{Yb}^{3+}/\text{Er}^{3+}$ (or Tm^{3+}) nanoparticles can be synthesized through thermal decomposition of sodium and lanthanide trifluoroacetates by using the single solvent of OM, which served both as a reaction medium and as a capping ligand [100]. However, the resulting hexagonal phase $\text{NaYF}_4:\text{Yb}^{3+}/\text{Er}^{3+}$ (or Tm^{3+}) upconversion nanoparticles had relatively poor shape. Subsequently, there was a series of excellent

reports on the thermolysis approach in using OA/OAM, OA/OAM/ODE, or OAM solvents to prepare monodispersed lanthanide-doped Eu_2O_3 [107], La_2O_3 [108], Gd_2O_3 [105, 106], LnOCl [102], LiYF_4 [111], and NaLnS_2 ($\text{Ln} = \text{La, Sm, Tb, Ce}$) [109] nanoparticles. The advantage of utilizing OAM for the preparation of up-conversion nanoparticles lied in its ability to produce ultrasmall upconversion nanoparticles that are attractive for bio-imaging due to their more efficient clearance from the body. In addition, the weak coordination bond between the amine group and the lanthanide ions on the surface of upconversion nanoparticles facilitated the utilization of a popular ligand exchange procedure for phase transfer.

Thermolysis in TOPO-based mixed solvents: Besides the most frequently used organic capping agents OA, OAM, and ODE, Shan et al. [113–115] first reported the use of TOPO as a coordinating ligand for the synthesis of ultrasmall, monodispersed, and pure hexagonal phase NaYF_4 upconversion nanoparticles. As compared to other available coordination solvents such as OA and OAM, the free-energy barrier for the cubic-to-hexagonal phase transition was significantly reduced in TOPO. Unfortunately, the solubility of the as-obtained TOPO-capped nanoparticles was low in common organic solvents such as cyclohexane or chloroform. This problem was solved by combined use of trioctylphosphine (TOP)/OA to replace TOPO to synthesize NaYF_4 nanoparticles. It was found that the cooperative actions of OA and TOP also could decrease the energy barrier of α/β phase transition, allowing the preparation of hexagonal NaYF_4 at lowered temperatures [113–115].

2.3.2 *Hydro(Solvo)Thermal Strategy*

The hydrothermal technique is becoming one of the most important tools for advanced materials processing, particularly owing to its advantages in the processing of nanostructural materials for a wide variety of technological applications such as electronics, optoelectronics, catalysis, ceramics, magnetic data storage, biomedical, and bio-photonics. The hydrothermal technique not only helps in processing monodispersed and highly homogeneous nanoparticles, but also acts as one of the most attractive techniques for processing nanohybrid and nanocomposite materials. The term “hydrothermal” is purely of geological origin. It was first used by the British geologist, Roderick Murchison (1792–1871), to describe the action of water at elevated temperature and pressure, in bringing about changes in the earth’s crust leading to the formation of various rocks and minerals.

Hydrothermal processing can be defined as any heterogeneous reaction in the presence of aqueous solvents or mineralizers under high pressure and temperature conditions to dissolve and recrystallize materials that are relatively insoluble under ordinary conditions. Definition for the word hydrothermal has undergone several changes from the original Greek meaning of the words “hydros” meaning water and “thermos” meaning heat. Recently, Byrappa and Yoshimura define hydrothermal as

any heterogeneous chemical reaction in the presence of a solvent (whether aqueous or non-aqueous) above the room temperature and at pressure greater than 1 atm in a closed system [134]. Possible advantages of this method over other types of synthetic methods include the ability to create highly crystalline phases at lower temperatures and to implement a set of reactions at the same time. Disadvantages of the method include the need for specialized reaction vessels known as autoclaves and the impossibility of observing the nanocrystal as it grows. The autoclaves usually consist of thick-walled steel cylinders with a hermetic seal for carrying out chemical reactions under pressure and high temperatures for prolonged periods of time. Furthermore, protective contact-type inserts typically made of Teflon and titanium materials are generally required to prevent solvent corrosion of the internal cavity of the autoclave.

In a typical procedure of hydro(solvo)thermal synthesis, appropriate reaction precursors, solvents, and surfactants with functional groups are mixed and then heated in a autoclaves. Surfactants such as polyethylenimine (PEI) [14], ethylenediaminetetraacetic acid (EDTA) [121], cetyltrimethylammonium bromide (CTAB), and OA provide chelating ability with cationic ions to regulate their reacting concentration [28], which are essential for the control of the crystalline phase, size, and morphology as well as the surface functional groups of resulting upconversion nanoparticles. The most representative example of hydro(solvo)thermal synthesis is provided by the work of Li and coworkers who reported on a general “liquid–solid-solution (LSS)” strategy for the synthesis of monodisperse (semiconductor, metallic, and dielectric) nanoparticles [37], whereby the reaction, phase transfer, and separation take place at the interfaces. Adapted from the LSS method, a variety of lanthanide-doped upconversion nanoparticles with well-controlled crystal phase, size, and shape have been synthesized, such as NaYF_4 [135–138], NaLaF_4 [28], NaLuF_4 [30, 130], BaGdF_5 [139], KMnF_4 [140], YF_3 [141–143], LaF_3 [28, 116, 117], LaOF [144], GdF_3 [116], CaF_2 [31], and SrF_2 [123]. Another interesting development was reported by Zhao and coworkers, who utilized an oleic acid-mediated hydrothermal method for the synthesis of uniform NaYF_4 nanorods, nanotubes, and flower-patterned nanodisks [34]. Very recently, Liu et al. developed a novel Gd^{3+} -doping approach to give simultaneous control over the crystal phase, size, and optical properties of the resulting NaYF_4 upconversion nanoparticles during the hydro(solvo)thermal synthesis [145]. It was discovered that Gd^{3+} doping not only resulted in a rapid cubic-to-hexagonal phase transformation within 2 h, but also lead to the reduction of size, producing ultra-small hexagonal NaYF_4 upconversion nanoparticles at a substantially decreased reaction temperature. The phase transformation and size and morphology optimization induced by impurity doping were further verified by some other groups. Li and coworkers reported the synthesis of $\text{NaLuF}_4:\text{Gd}^{3+}/\text{Yb}^{3+}/\text{Tm}^{3+}$ nanoparticles with controllable size and phase by doping different amounts of Gd^{3+} ions [146]. The addition of Gd^{3+} ions promoted the phase transformation from cubic to hexagonal and reduced the particle size from large microtubes to small cubes. Wang and coworkers extended this impurity doping strategy for the controlled synthesis of MF_2 ($\text{M} = \text{Ca}, \text{Sr}, \text{and Ba}$) and LnF_3 ($\text{Ln} = \text{La}, \text{Ce}, \text{and Pr}$) nanoparticles [123].

In addition to the aforementioned fluoride nanoparticles, monodispersed Ln^{3+} -doped inorganic oxide nanoparticles could also be readily obtained by using the hydro(solvo)thermal synthesis, as exemplified by the synthesis of Er_2O_3 [120], BaYF_5 [121], CeO_2 [122], NaYbF_4 [30, 116, 147], NaCeF_4 [125], Na_3MF_7 ($\text{M} = \text{Zr}$ or Hf) [127], YbPO_4 [21], LuPO_4 [21], KYF_4 [129], and NaLnF_4 ($\text{Ln} = \text{Pr}$, Nd , Sm , Eu , Gd , Dy , Ho , Er , Tm , Tb) [30].

2.3.3 Other Methods for the Synthesis of the Lanthanide-Doped Luminescent Nanoparticles

Coprecipitation is perhaps one of the most convenient techniques for synthesizing ultrasmall lanthanide-doped nanocrystals with narrow size distribution. Compared to other techniques, there is no need for costly equipment, stringent reaction conditions, and complex procedures, resulting in less time consumption. In some rare instances, crystalline nanoparticles were formed directly by coprecipitation, eliminating the need for a calcination step or post-annealing process. One of the earliest examples of this technique was demonstrated by van Veggel and coworkers [22], who made down-conversion LaF_3 nanocrystals doped with Ln^{3+} ($\text{Ln} = \text{Eu}$, Er , Nd , and Ho). The approach was expanded and refined by Chow and coworkers [18], who synthesized LaF_3 nanocrystals with smaller particle size (~ 5 nm) and narrower size distribution from simple water soluble inorganic precursors (Fig. 4a, b). In their studies, synthetic ammonium di-*n*-octadecyldithiophosphate was used as a capping ligand to control particle growth and to stabilize the nanocrystals against aggregation. These sub-10-nm crystals can be redispersed in solutions, offering promising applications as luminescent probes for bio-molecules with dimensions from several nanometres to tens of nanometres. In addition to LaF_3 nanocrystals, $\text{NaYF}_4\text{:Yb/Er}$ (Tm), $\text{LuPO}_4\text{:Yb/Tm}$, and $\text{YbPO}_4\text{:Er}$ nanocrystals were also synthesized via the coprecipitation approach coupled with heat treatment (or post-annealing process) for enhanced upconversion emission by the groups of Haase, Gudel, Chen, and Li [17, 19, 20, 21]. Commercially available ligands such as polyvinylpyrrolidone (PVP) and polyethylenimine (PEI) are also widely used to control particle growth and endow the nanocrystals with solubility and surface functionality [15, 16]. Particularly, the PEI-coated nanoparticles provide a platform for direct surface functionalization of bio-molecules by bio-conjugate chemistry [14].

Sol-gel processing is a typical wet-chemical technique for the fabrication of upconversion nanocrystals for applications as thin film coating and glass materials. The sol-gel process is characterized by the hydrolysis and polycondensation of metal alkoxide (or halide)-based precursors. To improve the crystallinity that is directly associated with luminescence efficiency of the nanocrystals, calcination at high temperatures is often needed. Prasad et al. [41] developed an interesting variation of the sol-gel method that produces Er^{3+} -doped ZrO_2 nanocrystals.

The method involved a sol-emulsion-gel technique that utilized reverse micelles formed in emulsions as the reactors for growing nanocrystals. The sol-gel process was also developed for a variety of upconversion nanocrystals with metal oxides as host materials including $\text{TiO}_2\text{:Er}$, $\text{BaTiO}_3\text{:Er}$, $\text{Lu}_3\text{Ga}_5\text{O}_{12}\text{:Er}$, and $\text{YVO}_4\text{:Yb/Er}$ [38–40]. Despite extensive research efforts in this area, the sol-gel-derived nanocrystals were not particularly suitable as luminescent probes for biological assays due to lack of particle size control and considerable aggregation of the particles when dispersed in aqueous solutions.

In stark contrast to sol-gel and hydro(solvo)thermal methods that often require heating for a prolonged time period up to several days at high temperatures to complete a synthesis, controlled explosions in reactions known as combustion synthesis can give reaction products in minutes. Once initiated by a heat source, highly exothermic reactions with temperatures ranging typically from 500 to 3,000 °C occur in the form of a combustion wave that propagates through the reaction materials in a self-sustained manner without requiring additional heat. The energy saving method represents one of the attractive techniques to synthesize a wide variety of oxide and oxysulfide upconversion nanocrystals (Y_2O_3 , $\text{La}_2\text{O}_2\text{S}$, and Gd_2O_3) reported by the groups of Capobianco, Luo, and Zhang [152–154].

2.3.4 Ultrasmall Upconversion Nanoparticles with Bright Upconversion Luminescence

Although upconversion nanoparticles show many advantages in the non-blinking property and high signal-to-noise ratio, however, compared with QDs and dyes, one of the biggest shortcomings is too large in size (~ 20 nm). The optimal size for bio-imaging probes is reported to be less than 10 nm, so that the nanoparticles can be efficiently cleared from the body. A few papers have reported the synthesis of the ultrasmall upconversion nanoparticles (Fig. 2.4). However, the low efficiency is often accompanied by the decrease in size. For example, it has been demonstrated that when the size was reduced to ~ 5 nm, the upconversion efficiency sharply declined to below 0.01 %, which is much lower than that of the particles with larger size. In regard to this, much effort has been input to obtain small (<10 nm) nanoparticles with intense upconversion emission and many positive achievements have been obtained [104, 148, 149, 155–157]. For example, Prasad’s group reported the synthesis of monodispersed $\text{NaYF}_4\text{:Yb}^{3+}/\text{Tm}^{3+}$ nanocrystals with ultrasmall size (7–10 nm) and high upconversion efficiency by thermolysis trifluoroacetate salts in the OA/OAM mixed solvents [104]. The intensity of NIR emission could be increased up to 43 times along with an increase in the relative content of Yb^{3+} ions from 20 to 100 %. The resultant ultrasmall $\text{NaYbF}_4\text{:2 %Tm}^{3+}$ nanocrystals manifest NIR photoluminescence emission, which was 3.6 times more

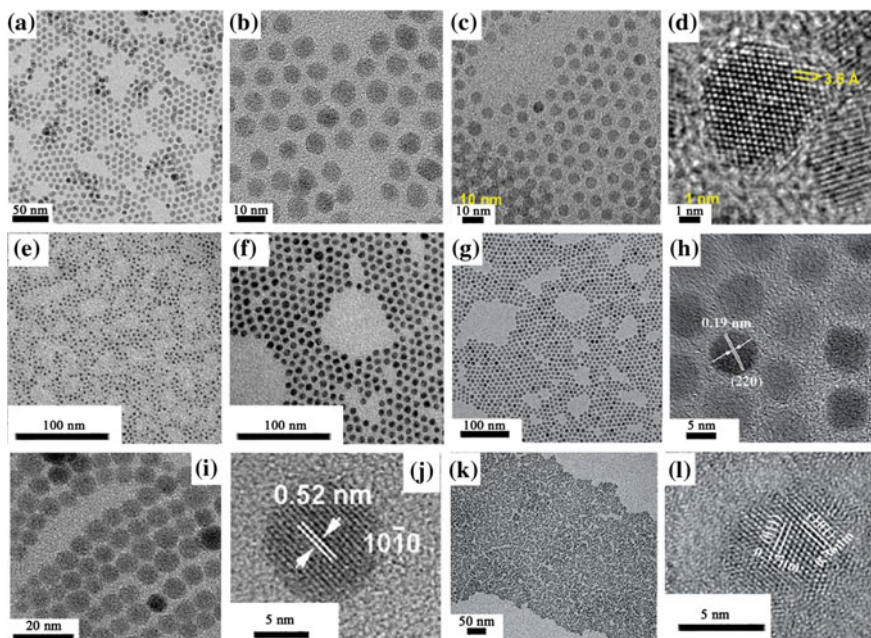


Fig. 2.4 TEM images of the ultrasmall (<10 nm) lanthanide-doped upconversion nanoparticles. **a, b** Cubic phase $\text{NaYF}_4\text{:Yb,Tm}$; **c, d** hexagonal phase $\text{NaYF}_4\text{:Yb,Er}$; **e, f** hexagonal phase NaGdF_4 ; **g, h** cubic phase $\text{CaF}_2\text{:Yb,Er@CaF}_2$; **i, j** $\text{NaLu}_x\text{Gd}_{1-x}\text{F}_4\text{:Yb,Er}$; **k, l** Orthorhombic $\text{YF}_3\text{:Yb,Er}$. **a, b** Reprinted with the permission from Ref. [104]. Copyright 2010 American Chemical Society. **c, d** Reprinted with the permission from Ref. [148]. Copyright 2012 American Chemical Society. **e, f** Reprinted with the permission from Ref. [149]. Copyright 2011 American Chemical Society. **g, h** Reprinted with the permission from Ref. [150]. Copyright 2013 Wiley-VCH Verlag GmbH & Co. KGaA. **i, j** Reprinted with the permission from Ref. [146]. Copyright 2011 American Chemical Society. **k, l** Reprinted with the permission from Ref. [151]. Copyright 2012 The Royal Society of Chemistry

intense than that from $\text{NaYF}_4\text{:20\%Yb}^{3+}/\text{2\%Tm}^{3+}$ nanocrystals with a size of 25–30 nm reported previously. Cohen's group also described the controlled synthesis of β -phase $\text{NaYF}_4\text{:20\%Yb}^{3+},\text{2\%Er}^{3+}$ nanocrystals with a protein size from 4.5 to 15 nm by using the thermolysis strategy in the OA/OAM/ODE solvents [148]. The core/shell β -phase $\text{NaYF}_4\text{:Yb}^{3+},\text{Er}^{3+}/\text{NaYF}_4$ nanoparticles less than 10 nm exhibited higher luminescence efficiency ($0.18 \pm 0.01\%$) than the core nanoparticles with 37 nm in size ($0.14 \pm 0.01\%$). Most recently, Liu et al. [146] also synthesized the sub-10-nm hexagonal NaLuF_4 , which displayed bright luminescence with a QY of $0.47 \pm 0.06\%$. Mahalingam et al. also demonstrated the upconversion process via interparticle energy transfer in Ln^{3+} -doped BaLuF_5 ($\text{Ln} = \text{Tm}$ and Yb) nanocrystals with a sub-5 nm size for the first time [156].

2.4 Synthesis Routes for the Fabrication of the Core@Shell Structured Upconversion Nanoparticles

In addition to Ln^{3+} -doped core-only nanoparticles, much progress has also been made in the synthesis of composite nanoparticles with core@shell structures in the past decade. Such composite core@shell nanoparticles not only provide an excellent platform to combine different functional units into one single nanoparticle, but also offer an effective solution to problems associated with the core-only nanoparticles such as low PL efficiency.

It has been demonstrated that the thermolysis strategy can offer precise control over the phase, shape, size, and stoichiometric composition of the upconversion nanocrystals. So the routes for the fabrication of the core@shell-structured upconversion nanocrystals are mainly based on thermolysis strategy. The thermolysis-based strategy for the fabrication of the core@shell upconversion nanocrystals can be divided into three routes: one-pot heating-up method for the synthesis of both core only and core@shell upconversion nanoparticles [158–161]; one-pot successive layer-by-layer (SLBL) [162–164] and Ostwald-ripening methods [56]. It should be noted that all the three routes are developed under the direction of the LaMer nucleation-growth model. So, in this section, we focus on the LaMer nucleation-growth model directed controllable synthesis of lanthanide-doped upconversion nanoparticles.

2.4.1 One-Pot Heating-Up Method

For one-pot heating-up method, the nucleation and growth match with the LaMer model for the synthesis of monodisperse upconversion nanoparticles. For the synthesis of the core upconversion nanoparticles, the precursors are mixed at a low temperature and then brought to the temperature at which precursor reaction or decomposition occurs sufficiently quickly to result in supersaturation (stage I). Supersaturation is again relieved by a “burst nucleation” (stage II), after which temperature is controlled to avoid additional nucleation events, allowing monomer addition to existing nuclei to occur more rapidly than new monomer formation (stage III).

The seed-mediated growth method for the synthesis of core@shell nanocrystals is the most apparent case for the separation of nucleation and growth, wherein nucleation is physically separated from growth by using preformed nanocrystals as seed nuclei. This method utilizes heterogeneous nucleation to suppress the formation of additional nuclei by homogeneous nucleation. In this method, the reaction can enter into stage III directly. Preformed nuclei are introduced into the reaction solution, and then the monomers are supplied to precipitate on the surface of the existing nuclei. The lower monomer concentration should be kept during growth to suppress homogeneous nucleation. So, the one-pot heating-up method can be used

not only in the synthesis of core-only nanoparticles but also make a great success in the fabrication of core@shell upconversion nanoparticles (Fig. 2.5a). The whole experiment procedure is nearly the same as the synthesis of the core nanoparticles except the presence of the seed nanoparticles. The first step is to synthesize the core nanoparticles which are then used as seeds in the second step to induce further epitaxial growth. To ensure an epitaxial growth and to create a homogeneous interface between the core and the outer shell, the host material of the shell should exhibit a low lattice mismatch with the core material. Then, the epitaxial growth can be implemented in the growth solution. The monomer of shells in the growth solution, produced by thermal decomposition of corresponding chemical precursors in the solvents of OA and ODE, is able to gradually and stably deposit on the seeding core nanoparticles and finally form the shell layer (stage III in LaMer plot).

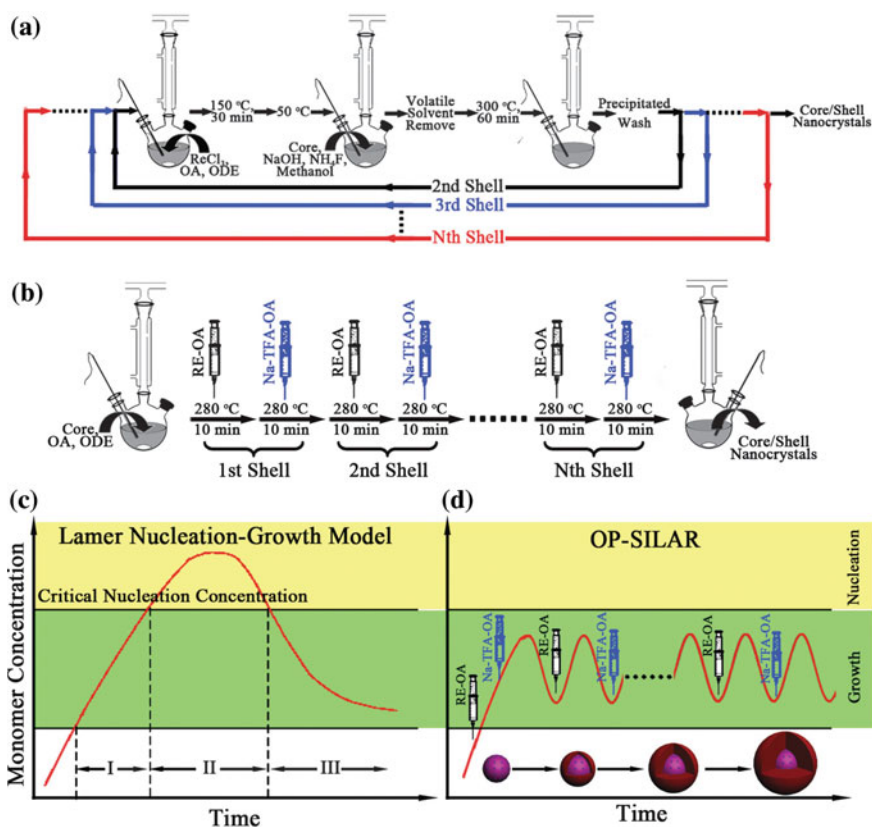


Fig. 2.5 a, b Schematic depiction of conventional heating-up multi-cycle method (a) and the SLBL method (b) for the synthesis of core@shell upconversion nanoparticles. c, d Schematic illustration of the LaMer plot and the SLBL method for the controlled synthesis of core@shell upconversion nanoparticles by using the SLBL method. a–d Reprinted with the permission from Ref. [164]. Copyright 2013 American Chemical Society

2.4.2 Successive Layer-by-Layer Strategy for the Fabrication of Multi-shell-Structured Upconversion Nanoparticles

Although one-pot heating-up method has been considered to the most commonly used method for the fabrication of core@shell upconversion nanoparticles, a few shortcomings should still be improved. For example, recent work by van Veggel et al. showed that the core@shell nanoparticles synthesized by the one-pot heating-up method did not have a uniform shell (the core is only partially covered by shell), indicating that the core nanoparticles could not be passivated efficiently to decrease the core surface defects and insulated from the environmental effect [161, 165]. On the other hand, it was found that the size distribution of the obtained core@shell nanoparticles was larger than that of the original core. Furthermore, bimodal size distribution is always observed when a high volume of shell precursors is introduced [158]. It is assumed that the non-uniform shell and broader or bimodal size distribution of the obtained core@shell upconversion nanoparticles is resulted from the fast deposition speed or independent nucleation of the shell precursors induced by excessive introducing of the shell precursors. Although a homogeneous shell could be obtained by using the multi-cycle path (reducing the amount of shell precursors of each cycle) (Fig. 2.5a) [159], owing to the selection of the low boiling point NaOH-NH₄F-methanol precursor, the multi-cycle path must undergo a lengthy cooling and volatile solvent removing process during the growth of every layer of shell. For the reason of batch operation, this process is considered to be time-consuming, laborious, and user unfriendly, especially for the synthesis of complicated multi-shell upconversion nanoparticles. Based on the LaMer nucleation-growth model [10, 60], our group developed a facile one-pot successive layer-by-layer method to realize the successive shell coating by using high boiling-point Re-OA and Na-TFA-OA as a shell precursor (Fig. 2.5b) [164]. This protocol was flexible to deposit uniform multi-shell by successive introducing of the shell precursor solutions instead of the lengthy multi-cycle batch operation. This protocol was flexible to deposit uniform multi-shell on both hexagonal and cubic phase cores by successive introducing of the shell precursor solutions. The shell thickness of nanoparticles could be well controlled from 1 ML (~ 0.36 nm) to more than 20 ML (~ 8 nm) by simply tuning the amounts of the shell precursors. Furthermore, the tunable doping positions (core and shell doping) could also be achieved by adjusting the species and addition sequence of the shell precursors. With SLBL method, the preformed nuclei were dissolved into the reaction solution and then the shell precursors were alternately introduced, and the formed monomers were supplied to precipitate on the surface of the nuclei. The monomer concentration was kept low during the growth to suppress homogeneous nucleation because its production and consumption maintained the balance. The released monomers could be continuously consumed to deposit as a shell without homogeneous nucleation (Fig. 2.5c). The most distinguished feature of core@shell upconversion nanoparticles synthesized from SLBL method was that the shell was

very uniform. It means that the cores were completely covered by shell, which is quite different from the non-uniform shell nanoparticles synthesized by commonly used one-pot heating-up method (the core was only partially covered by shell). As a result of the high-quality uniform shells, the optical properties of the obtained core@shell nanoparticles could be improved in upconversion luminescence efficiency and stability. Most recently, our group reported for first time that the homogeneous doping approach based on the SLBL method could greatly improve the efficiency of the upconversion nanoparticles [166]. The quantum yield as high as $0.89 \pm 0.05 \%$ was realized for the homogeneous doping $\text{NaGdF}_4:\text{Yb,Er}/\text{NaYF}_4$ upconversion nanoparticles, which was nearly 2 times higher than that of the heterogeneous doping $\text{NaGdF}_4:\text{Yb,Er}/\text{NaYF}_4$ upconversion nanoparticles ($0.47 \pm 0.05 \%$). The influences of spatial distributions and local relative concentrations of the dopants on the optical properties of upconversion nanoparticles were investigated in the single particle level. It was found that heterogeneous doping indeed existed during the spontaneous growth process of the nanoparticles. The heterogeneous doping property can further induce many negative effects on the optical properties of upconversion nanoparticles, especially the luminescent efficiency. The spatial distributions and local relative concentrations of the dopants can be well controlled by the SLBL homogeneous doping method on the monolayer level and homogeneously distributed in the single particle level. With the similar SLBL method, the highly efficient $\text{LiLuF}_4:\text{Ln}^{3+}@\text{LiLuF}_4$ core@shell upconversion nanoparticles and dual-mode up/down converting $\text{NaGdF}_4:\text{Nd}@\text{NaYF}_4@\text{NaGdF}_4:\text{Nd, Yb, Er}@\text{NaYF}_4$ core@shell1@shell2@shell3 has been well established [162, 163].

As mentioned above, the SLBL method can realize the monolayer control of the shell thickness. The spherical concentric shell model (CSM) can be employed to calculate the amount of shell precursor necessary for the growth of each monolayer (ML) [159, 167]. This model has been used extensively for the hexagonal CdS and ZnS shell deposition during the core-shell nanocrystal synthesis process [167]. Because of the highly symmetric structure of the CdS, the ML was inferred to a thickness equal to half the length of the *c*-lattice parameter. Although the NaGdF_4 shell adopted here has also hexagonal structure ($P6_3/m$, $a = 6.02 \text{ \AA}$, $c = 3.60 \text{ \AA}$), the cation sites are of three types. A onefold site occupied by RE^{3+} , another site occupied randomly by $1/2\text{Na}^+$ and $1/2\text{RE}^{3+}$, and a twofold site occupied randomly by Na^+ and vacancies [145, 159]. Therefore, referral to a NaGdF_4 , the ML could be taken to mean a thickness equal to the *c*-lattice parameter of the bulk material, 0.36 nm in the case of the hexagonal NaGdF_4 . The required Gd-OA precursor amount for every layer of one particle can be calculated by the following equations:

$$\begin{aligned} m_{\text{layer}(n)} &= m_{\text{particle}(n)} - m_{\text{particle}(n-1)} = \rho(V_{\text{particle}(n)} - V_{\text{particle}(n-1)}) \\ &= \rho \frac{4}{3} \pi (r_{\text{particle}(n)}^3 - r_{\text{particle}(n-1)}^3) \end{aligned} \quad (2.28)$$

Density of the NaGdF_4 materials (ρ) is calculated as follows:

$$\rho = \frac{m}{V} = \frac{M}{\left(N_A * c * \frac{\sqrt{3}}{2} a^2\right) / N'} \quad (2.29)$$

Here M represents relative molecular mass of the material of NaGdF_4 , N' means the number of NaGdF_4 units that one crystal cell contains and according to crystal structure of the hexagonal NaGdF_4 , $N' = 1.5$. So, for NaGdF_4 , the cell parameter is $a = 6.02 \text{ \AA}$, $c = 3.60 \text{ \AA}$, molecular weight (M) = 256.3, and $\rho = 5.65 \text{ g/cm}^3$. For NaYF_4 , cell parameter is $a = 5.96 \text{ \AA}$, $c = 3.53 \text{ \AA}$, molecular weight $M = 187.9$, and $\rho = 4.31 \text{ g/cm}^3$.

Particle number of one molar (N) the NaGdF_4 (N) is calculated as follows:

$$N = \frac{V_{\text{per molar}}}{V_{\text{per particle}}} = \frac{\frac{M_0}{\rho_0}}{\frac{4}{3} \pi r_0^3} \quad (2.30)$$

Because the particle number is constant during the particle growth from smaller to bigger, the particle number of the obtained initial seeds is nearly the same as N .

2.4.3 Ostwald Ripening Strategy for the Fabrication of Core@Shell Upconversion Nanoparticles

The Ostwald-ripening process is referred to the last stage in LaMer plot, in the process larger particles with smaller surface-to-volume ratios are favored over energetically less stable smaller particles, resulting in the growth of larger particles at the expense of smaller ones. The fabrication of core@shell upconversion nanoparticles by using the common physical phenomenon of Ostwald ripening (i.e., self-focusing by Ostwald ripening) was developed by van Veggel and coworkers [56]. In their study, small $\alpha\text{-NaYF}_4$ sacrificial nanoparticles (SNPs) were synthesized first and then used as shell precursors. The subsequent injection of SNPs into a hot solution of NaYF_4 core nanoparticles (defocusing) can induce the rapid dissolution of SNPs and their deposition onto the larger core nanoparticles (self-focusing), thereby resulting in the formation of genuine core@shell-structured upconversion nanoparticles with a well-defined shape, narrow size distribution, and tunable shell growth. More importantly, the shell thickness and multiple layers of such core@shell upconversion nanoparticles can be precisely controlled by manipulating the number of SNPs injected and/or repeating the above defocusing and self-focusing cycle. Furthermore, this method is flexible and can be easily extended to prepare other high-quality core@shell nanoparticles with different compositions.

2.4.4 Cation Exchange Strategy for the Fabrication of Core@Shell Upconversion Nanoparticles

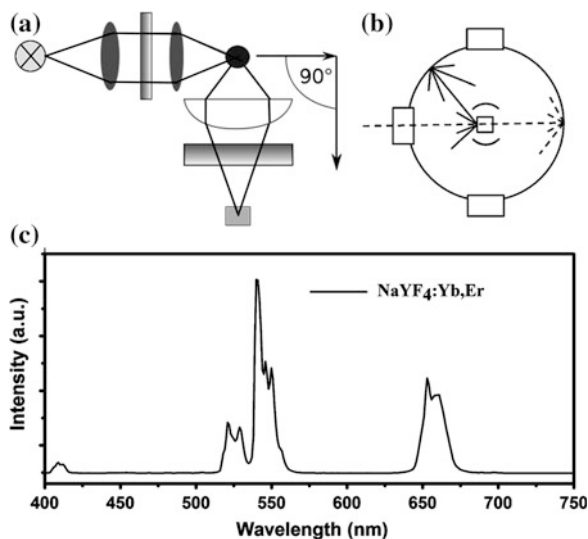
Besides the self-focusing by Ostwald-ripening strategy, another facile way to prepare monodisperse Ln^{3+} -doped core@shell nanoparticles is through a cation exchange reaction. One of the earliest examples of this technique was demonstrated by van Veggel and Dong [168], who prepared $\text{GdF}_3@ \text{LnF}_3$ core@shell nanoparticles by exposing GdF_3 core nanoparticles to an aqueous solution containing excess Ln^{3+} ions, where the Gd^{3+} ions in GdF_3 nanoparticles were partially replaced by the Ln^{3+} in the solution. By refining this synthetic route, they synthesized multifunctional $\text{NaYF}_4:\text{Yb}/\text{Tm}@ \text{NaGdF}_4$ core@shell nanoparticles with tunable shell thickness, enhanced upconversion luminescence and outstanding paramagnetic performance via cation exchange of $\text{NaYF}_4:\text{Yb}/\text{Tm}$ nanoparticles with Gd^{3+} ions, making these nanoparticles promising for bimodal imaging, namely, optical bio-imaging and magnetic resonance imaging (MRI) [165]. Similarly, Li and coworkers developed a novel approach based on rare earth cation-assisted ligand assembly to synthesize Gd^{3+} -modified $\text{NaYF}_4:\text{Yb}/\text{Er}$ core@shell nanoparticles [169]. In their study, $\text{NaYF}_4:\text{Yb}/\text{Er}$ nanoparticles were first synthesized via a modified cothermolysis process in oleylamine, then Gd^{3+} ions were introduced onto the surface of the $\text{NaYF}_4:\text{Yb}/\text{Er}$ nanoparticles by cation-assisted ligand assembly, which thereby greatly increased the positive charge on the surface of the $\text{NaYF}_4:\text{Yb}/\text{Er}$ nanoparticles so that the functional molecules (i.e., folic acid and aminocaproic acid) can be attached.

2.5 Characterizations

2.5.1 Optical Characterization

The most direct and immediate probes for upconversion nanoparticles are the fluorescence spectra. In a typical fluorescence (emission) measurement (Fig. 2.6a), the excitation wavelength is fixed and the detection wavelength varies. Two general types of instruments exist: (1) Filter fluorometers use filters to isolate the incident light and fluorescent light. (2) Spectrofluorometers use diffraction grating monochromators to isolate the incident light and fluorescent light. Both types use the following scheme: The light from an excitation source passes through a filter or monochromator and strikes the sample. A proportion of the incident light is absorbed by the sample and some of the molecules in the sample fluoresce. The fluorescent light is emitted in all directions. Some of this fluorescent light passes through a second filter or monochromator and reaches a detector, which is usually placed at 90° to the incident light beam to minimize the noise created from radiant power fluctuations and the risk of transmitted or reflected incident light reaching the detector.

Fig. 2.6 **a** Scheme illustration of the fluorescence spectroscopy. **b** Diagram of the integrating sphere setup for luminescence measurements. *Dashed line* excitation light; *solid line* sample emission. **c** Typical upconversion emission spectra of the $\text{NaYF}_4\text{:Yb,Er}$ upconversion nanocrystals



As mentioned before, the fluorescence is most often measured at a 90° angle relative to the excitation light. This geometry is used instead of placing the sensor at the line of the excitation light at a 180° angle in order to avoid interference of the transmitted excitation light. No monochromator is perfect and it will transmit some stray light, that is, light with other wavelengths rather than the targeted. An ideal monochromator would only transmit light in the specified range and have a high wavelength-independent transmission. When measuring at a 90° angle, only the light scattered by the sample causes stray light. This results in a better signal-to-noise ratio, and lowers the detection limit by approximately a factor of 10,000, when compared to the 180° geometry. Furthermore, the fluorescence can also be measured from the front, which is often done for turbid or opaque samples. The detector can either be single-channeled or multi-channeled. The single-channeled detector can only detect the intensity of one wavelength at a time, while the multi-channeled detects the intensity of all wavelengths simultaneously, making the emission monochromator or filter unnecessary. The different types of detectors have both advantages and disadvantages.

In traditional commercial available fluorescence spectroscopy, xenon arcs and mercury-vapor lamps light sources are always used as excitation sources. A mercury-vapor lamp is a line lamp, meaning it emits light near peak wavelengths. By contrast, a xenon arc has a continuous emission spectrum with nearly constant intensity in the range from 300 to 800 nm and a sufficient irradiance for measurements down to just above 200 nm. Filters and/or monochromators may be used to get the excitations with narrow wavelength interval. A monochromator transmits light of an adjustable wavelength with an adjustable tolerance. The most common type of monochromator utilizes a diffraction grating, that is, collimated light illuminates a grating and exits with a different angle depending on the wavelength.

The monochromator can then be adjusted to select which wavelengths to transmit. For allowing anisotropy measurements, the addition of two polarization filters is necessary: One after the excitation monochromator or filter, and one before the emission monochromator or filter. For the fluorescence spectroscopy used in the measurement of upconversion nanomaterials, the excitation sources should be replaced by a NIR laser (~ 980 , 800 nm etc.) which can only emits light of high irradiance at a very narrow wavelength interval. Because (1) the xenon arc has a continuous emission spectrum range from 300 to 800 nm, which cannot be used as the excitation source of upconversion nanomaterials; (2) the power density of the narrow wavelength excitation, which is obtained from the xenon arc by using filters and/or monochromators, is too low to excite the upconversion luminescence. The excitation monochromator or filter is unnecessary when a laser is used as the excitation source. Figure 2.6c shows the typical upconversion emission spectra of the $\text{NaYF}_4\text{:Yb,Er}$ upconversion nanocrystals.

Unlike in UV/visible spectroscopy, “standard”, device-independent spectra are not easily attained. Several factors influence and distort the spectra, and corrections are necessary to attain “true”, i.e., machine-independent, spectra. The different types of distortions will here be classified as being either instrument- or sample-related. Firstly, the distortion arising from the instrument is discussed. As a start, the light source intensity and wavelength characteristics varies over time during each experiment and between each experiment. Furthermore, no lamp has a constant intensity at all wavelengths. To correct this, a beam splitter can be applied after the excitation monochromator or filter to direct a portion of the light to a reference detector. Additionally, the transmission efficiency of monochromators and filters must be taken into account. These may also change over time. The transmission efficiency of the monochromator also varies depending on wavelength. This is the reason that an optional reference detector should be placed after the excitation monochromator or filter. The percentage of the fluorescence picked up by the detector is also dependent upon the system. Furthermore, the detector quantum efficiency, that is, the percentage of photons detected, varies between different detectors, with wavelength and with time, as the detector inevitably deteriorates.

Two other topics that must be considered including the optics used to direct the radiation and the means of holding or containing the sample material (called a cuvette or cell). For most UV, visible, and NIR measurements, the use of precision quartz cuvettes is necessary. In both cases, it is important to select materials that have relatively little absorption in the wavelength range of interest. Quartz is ideal because it transmits from 200 to $2,500$ nm; higher grade quartz can even transmit up to $3,500$ nm, whereas the absorption properties of other materials can mask the fluorescence from the sample. Correction of all these instrumental factors for getting a “standard” spectrum is a tedious process, which is only applied in practice when it is strictly necessary. This is the case when measuring the quantum yield or when finding the wavelength with the highest emission intensity for instance.

As mentioned earlier, distortions arise from the sample as well. Therefore, some aspects of the sample must be taken into account too. Firstly, photodecomposition may decrease the intensity of fluorescence over time. Scattering of light must also

be taken into account. The most significant types of scattering in this context are Rayleigh and Raman scattering. Light scattered by Rayleigh scattering has the same wavelength as the incident light, whereas in Raman scattering the scattered light changes wavelength usually to longer wavelengths. Raman scattering is the result of a virtual electronic state induced by the excitation light.

Frequently, the upconversion emission spectra were used in the qualitative analysis of the upconversion nanocrystals. It is very hard to get the quantitative information from the upconversion emission spectra, especially for the spectra obtained from different equipments or samples. For comparison, the integrating sphere is always used to quantify the intensity of fluorescence. An integrating sphere (also known as an Ulbricht sphere) is an optical component consisting of a hollow spherical cavity with its interior covered with a diffuse white reflective coating, with small holes for entrance and exit ports (Fig. 2.6b). Its relevant property is a uniform scattering or diffusing effect. Light rays incident on any point on the inner surface are, by multiple scattering reflections, distributed equally to all other points. The effects of the original direction of light are minimized. An integrating sphere may be thought of as a diffuser which preserves power but destroys spatial information. It is typically used with some light source and a detector for optical power measurement. It has become a standard instrument in photometry and radiometry. It has the advantage over a goniophotometer for measuring the light produced by a source that total power can be obtained in a single measurement.

Until now, the low upconversion efficiencies of upconversion nanoparticles are still the most serious limitation for commercialization, resulting that in most of applications having to be operated at high excitation densities. The efficiency of an upconverter is determined by many variables which influence the radiative, non-radiative, and energy transfer rates, e.g., phonon energies, spectral overlap between sensitizer emission and activator absorption, temperature, and defects that quench the emission. Very importantly, as upconversion is a nonlinear process, the efficiency strongly depends on excitation power. This makes it difficult to define the upconversion efficiency detected under different conditions. There is no generally accepted definition on upconversion efficiency. When the efficiency is determined, it is still not clear how to interpret the values reported. For example, for one emitted photon, at least two photons are absorbed. This means that the maximum internal quantum efficiency is 50 %, analogous to the fact that downconversion can have an efficiency of 200 %. Still, sometimes this maximum efficiency is reported as 100 %.

In 2010, van Veggel et al. reported the measurement of absolute efficiencies of upconversion nanoparticles by using the integrating sphere [155]. They employed a barium sulfate-coated integrating sphere (150 mm in diameter) from Edinburgh instruments. The integrating sphere was mounted on the fluorimeter with the entry and output ports of the sphere located in 90° geometry from each other in the plane of the spectrometer. The powder or colloidal samples were held in a quartz cuvette located in the center of the integrating sphere. Samples were excited with a ~980 nm laser diode coupled to a 105-μm fiber. The emission from the fiber tip was collimated to a beam diameter of 1 mm and directed on the samples using a fiber coupler. Baffles were employed on both sides of the sample holder to ensure

that no scattered excitation light or emissions would be collected before scattering off the inside of the sphere. All the spectroscopic data collected were corrected for the spectral response of both the fluorimeter and the integrating sphere. The response of the detection systems in photon flux (sphere, monochromators, and detectors) was determined using a calibrated tungsten lamp. These normalization curves were then applied to all measured spectra.

The QY is defined as:

$$QY = \frac{\text{Photons emitted}}{\text{Photons absorbed}} = \frac{L_{[\text{sample}]}}{E_{[\text{reference}]} - E_{[\text{sample}]}} \quad (2.31)$$

where QY is the quantum yield, L_{sample} is the emission intensity, $E_{\text{reference}}$ and E_{sample} are the intensities of the excitation light not absorbed by the sample and the reference sample, respectively. The above equation expresses the number of photons emitted (numerator) divided by the number of photons absorbed (denominator), so it runs from 0 to 100 % for a one-photon processes and from 0 to 50 % for a two-photon processes.

According to the above method reported by Boyer and van Veggel, an increasing number of papers began to involve data of the efficiency (Table 2.2). For example, Liu et al. [146] reported that hexagonal NaLuF₄ nanocrystals codoped with Gd³⁺, Yb³⁺, and Er³⁺ with sub-10 nm size displayed bright luminescence with a QY of 0.47 ± 0.06 % under the excitation laser at 980 nm. Cohen et al. reported on the controlled synthesis of protein-sized (4.5–15 nm) β -NaYF₄:Yb³⁺,Er³⁺ nanocrystals with the efficiency as high as 0.18 ± 0.01 % [148]. As a result of the high-quality uniform multi-shell epitaxial growth by using the one-pot successive layer-by-layer (SLBL) strategy developed by our group, the optical properties of the obtained core-shell nanocrystals could be highly improved in upconversion luminescence efficiency (up to 0.51 ± 0.08 %) [164]. Prasad's group realized the efficiency as high as $\sim 1.2 \pm 0.1$ % under the excitation of 1,490 nm for the green photoluminescence of NaYF₄:Yb³⁺,Er³⁺ nanocrystals [94]. It is almost four times higher than the photoluminescence efficiency reported to date for hexagonal NaYF₄:Yb³⁺,Er³⁺ with a size of ~ 100 nm using excitation at ~ 980 nm, but it is still lower than the bulk materials. In 2012, Xu et al. [170] reported that the NaYF₄:Yb,Tm@NaYF₄ upconversion nanoparticles showed the QY of 3.5 % for 800 nm emission under excitation intensity of 78 W/cm². At a low excitation intensity of 21.7 mW/cm², the QY was determined to be 3.8×10^{-4} . Although this is the highest efficiency reported to date in literatures for the upconversion nanoparticles, QY measurement method and the detected emission wavelength are different from those reported by van Veggel et al. [155]. In this work, the standard fluorophores were employed to measure the QY with the integrating sphere-based system. The resulting QY of the upconversion nanoparticles was calculated by an indirect comparison. So the upconversion efficiency results should be interpreted with caution and further studies of the efficiency of upconversion nanoparticles are certainly needed in the future work.

Table 2.2 The efficiency of the upconversion nanoparticles with different crystal structure, size, and excitation power reported in the literatures

Upconversion nanoparticles	Crystal structure	Average size (nm)	Power density (W/cm ²)	Efficiency (%)	References
NaYF ₄ :20%Yb ³⁺ , 2%Er ³⁺	Hexagonal	Bulk	20	3.0 ± 0.3	[155]
NaYF ₄ :20%Yb ³⁺ , 2%Er ³⁺	Hexagonal	100	150	0.30 ± 0.10	[155]
NaYF ₄ :20%Yb ³⁺ , 2%Er ³⁺	Hexagonal	30	150	0.10 ± 0.05	[155]
NaYF ₄ :20% Yb ³⁺ , 2%Er ³⁺	Hexagonal	8–10	150	0.005 ± 0.005	[155]
NaYF ₄ :20%Yb ³⁺ , 2%Er ³⁺ @NaYF ₄	Hexagonal	30	150	0.30 ± 0.10	[155]
NaLuF ₄ :24%Gd ³⁺ , 20%Yb ³⁺ , 1% Tm ³⁺	Hexagonal	7.8	17.5	0.47 ± 0.06	[146]
NaYF ₄ :20%Yb, 2%Er	Hexagonal	5.4	1,000	0.0022 ± 0.0001	[148]
NaYF ₄ :20%Yb, 2%Er@NaYF ₄	Hexagonal	9	1,000	0.18 ± 0.01	[148]
NaYF ₄ :20%Yb, 2%Er	Hexagonal	37	1,000	0.14 ± 0.01	[148]
NaGdF ₄ :20%Yb, 2%Er	Hexagonal	5	100	0.016 ± 0.008	[164]
NaGdF ₄ :20%Yb, 2%Er @NaYF ₄	Hexagonal	17	100	0.51 ± 0.01	[164]
LiYF ₄ :Er ³⁺	Tetragonal	85	–	1.2 ± 0.1	[94]
NaYF ₄ :Yb, Tm@NaYF ₄	Hexagonal	42	78	3.5	[170]

2.5.2 Chemical and Structural Characterization

2.5.2.1 Transmission Electron Microscopy

One of the typical characters of the upconversion nanomaterials is the small particle size. Although some structural features can be revealed by X-ray and neutron diffraction, direct imaging of nanoparticles is only possible using transmission electron microscopy (TEM) and scanning probe microscopy. TEM is unique because it can provide a real space image of the atomic distribution in the nanocrystals and on their surface. Today's TEM is a versatile tool that provides not only atomic-resolution lattice images, but also chemical information at spatial resolution of 1 nm or better, allowing direct identification the chemistry of a single nanocrystal.

A TEM is composed of an illumination system, a specimen stage, an objective lens system, a magnification system, a data recording system, and a chemical analysis system. In addition to the morphology information, TEM can also provide us information about the crystal structure by the selected area electron diffraction (SAED), the chemical composition and distribution of the nanoparticles by the chemical analysis system. The chemical analysis system is making use of the energy-dispersive X-ray spectroscopy (EDS) and the electron energy-loss spectroscopy (EELS), both can be used complimentary to quantify the chemical composition of the specimen. EELS can also provide information about the electronic structure of the specimen.

SAED is a crystallographic experimental technique that can be performed inside a TEM. In a TEM, a thin crystalline specimen is subjected to a parallel beam of high-energy electrons. As TEM specimens are typically ~ 100 nm thick, and the electrons typically are accelerated with the energy of 100–400 kV, allowing them to pass through the electrons pass through the sample easily. In this case, electrons are treated as wave-like, rather than particle-like (wave-particle duality). Because the wavelength of high-energy electrons is a few thousandths of a nanometer, and the spacing between atoms in a solid is about a hundred times larger, the atoms act as a diffraction grating to the electrons, which are diffracted. That is, some fraction of them will be scattered to particular angles, determined by the crystal structure of the sample, while others continue to pass through the sample without deflection. As a result, the image on the screen of the TEM will be a series of spots, i.e., the selected area diffraction pattern, each spot corresponding to a satisfied diffraction condition of the sample's crystal structure. If the sample is tilted, the same crystal will stay under illumination, but different diffraction conditions will be activated, and different diffraction spots will appear or disappear. Figure 2.7a shows the typical SAED of the hexagonal and cubic phase NaYF_4 nanoparticles [164]. It can be seen that the two SAED show quite different diffraction rings. Figure 2.7a1 shows four distinct rings and the calculated d -spacings matched well with interplanar distances of (111), (200), (220), and (311) planes of cubic phase NaYF_4 (JCPDS, 77-2042). In contrast, the d -spaces of the lattice planes measure from Fig. 2.7a2 are

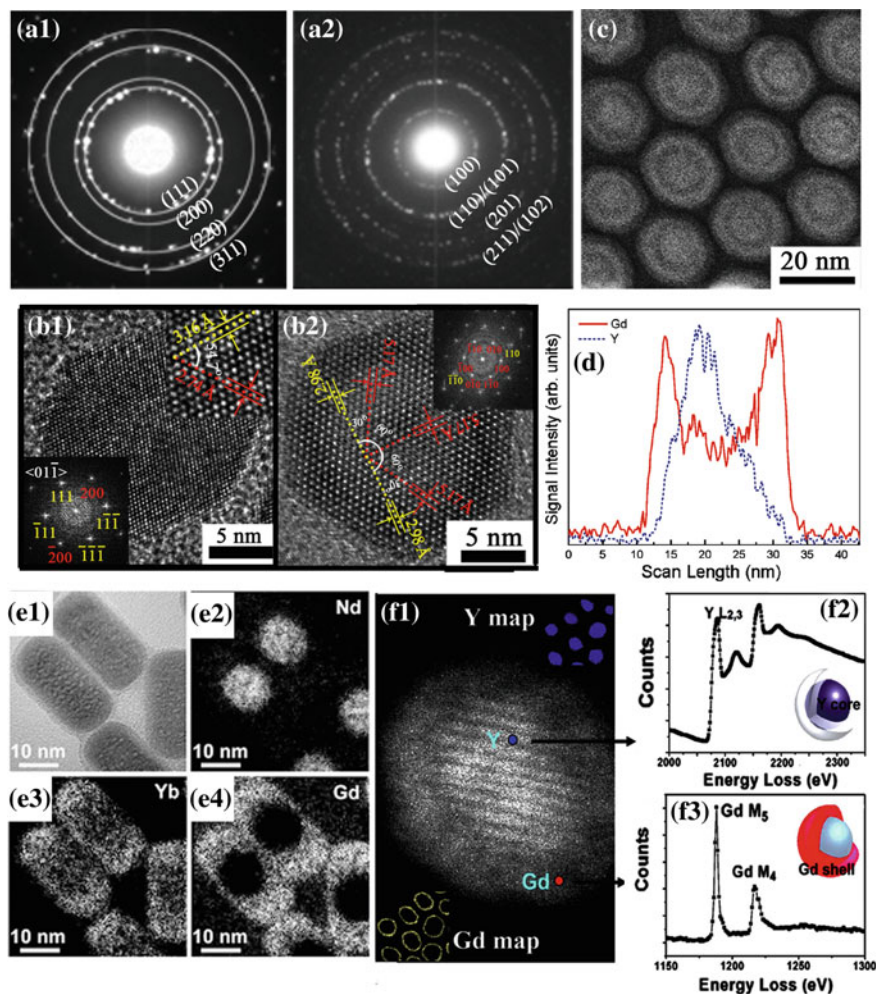


Fig. 2.7 **a** Typical selected area electron diffraction of cubic phase **(a1)** and hexagonal phase **(a2)** NaYF_4 . **b** Typical high-resolution transmission electron microscopy images of cubic phase **(b1)** and hexagonal phase **(b2)** NaYF_4 . **c** Typical HAADF-STEM image of the core@shell1@shell2@shell3-structured $\text{NaGdF}_4/\text{NaYF}_4/\text{NaGdF}_4/\text{NaYF}_4$ nanocrystals. **d** Energy-dispersive X-ray spectroscopy line scan across a single $\text{NaYF}_4/\text{NaGdF}_4$ core@shell NC showing Y in the core of the particle and Gd located in the shell. **e** Element maps of Nd, Yb, and Gd in the $\text{NaYbF}_4:\text{Nd}@\text{Na}(\text{Yb}, \text{Gd})\text{F}_4:\text{Er}@\text{NaGdF}_4$ nanoparticles. **f** HADDF image of a single $\text{NaYF}_4:\text{Yb}, \text{Er}@\text{NaGdF}_4$ nanocrystal **(f1)** and the corresponding EELS spectra of yttrium $L_{2,3}$ **(f2)** and gadolinium $M_{4,5}$ **(f3)** edges taken from the probe location on the inferred $\text{NaYF}_4:\text{Yb}, \text{Er}$ core and NaGdF_4 shell. **a, b** Reprinted with the permission from Ref. [164]. Copyright 2013 American Chemical Society. **c** Reprinted with the permission from Ref. [162]. Copyright 2013 Nature Publishing Group. **d** Reprinted with the permission from Ref. [161]. Copyright 2011 American Chemical Society. **e** Reprinted with the permission from Ref. [171]. Copyright 2013 Wiley-VCH Verlag GmbH & Co. KGaA. **f** Reprinted with the permission from Ref. [159]. Copyright 2012 American Chemical Society

corresponding to the lattice parameters of the (100), (110)/(101), (201), and (211)/(102) planes of β phase NaYF_4 (JCPDS, 16-0334).

High-resolution transmission electron microscopy (HRTEM) is an imaging mode of the TEM that allows for direct imaging of the atomic structure of the sample. HRTEM is a powerful tool to study properties of materials on the atomic scale. Figure 2.7b shows the typical HRTEM images of the hexagonal and cubic phase NaGdF_4 nanoparticles [164]. It can be seen that the two particles show quite different crystal lattices. The d -spaces of the lattice planes measure from Fig. 2.7b1 are ~ 2.7 and ~ 3.2 Å, with an angle of the two planes $\sim 55^\circ$, corresponding to the lattice parameters of the (111) and (200) planes of α phase NaGdF_4 . The d -spaces of the lattice planes measure from Fig. 2.7b2 are ~ 5.1 and ~ 3.0 Å, with an angle of the two planes $\sim 30^\circ$, corresponding to the lattice parameters of the (100) and (110) planes of β phase NaGdF_4 . The results are consistent with the above-mentioned SAED.

As mentioned above, the core@shell structure is one of the most important structures of the upconversion nanoparticles. However, the core-shell structure is commonly inferred from optical measurements, but problems with this arise because luminescence measurements give no insight into the mechanism of shell growth or coverage. Standard TEM is unable to differentiate between core and shell materials in lanthanide-based NCs because of similar material lattice constants and very little contrast difference between core and shell materials. Scanning transmission electron microscopy (STEM), coupled to techniques such as EELS and EDS, is well suited to the characterization of materials with complex compositions on the nanoscale, providing both structural and chemical information. A STEM is a type of TEM. As with any transmission illumination scheme, the electrons pass through a sufficiently thin specimen. However, STEM is distinguished from conventional TEM by focusing the electron beam into a narrow spot which is scanned over the sample in a raster. The rastering of the beam across the sample makes these microscopes suitable for analysis techniques such as mapping by energy-dispersive EDX spectroscopy, EELS, and high-angle annular dark-field imaging (HAADF). These signals can be obtained simultaneously, allowing direct correlation of image and quantitative data. By using HAADF-STEM, it is possible to form atomic-resolution images where the contrast is directly related to the atomic number (Z -contrast image). The directly interpretable Z -contrast image makes STEM imaging with a high-angle detector appealing, especially for the determination of the core@shell structure. Figure 2.7c shows a typical HAADF-STEM image of the core@shell1@shell2@shell3-structured $\text{NaGdF}_4/\text{NaYF}_4/\text{NaGdF}_4/\text{NaYF}_4$ nanocrystals [162]. It can be seen that the nanocrystals show clearly multilayer sandwich structure (bright-dark-bright-dark) in which the brighter parts correspond to the heavier Gd elements ($Z = 64$) and the darker parts correspond to the lighter Y elements ($Z = 39$).

As the aforementioned, we can only judge the formation of the core@shell structure from the contrast difference of the HAADF-STEM images. More characterizations are needed to obtain the chemical compositions of the core@shell nanoparticles. Energy-dispersive X-ray spectroscopy (EDS, EDX, or XEDS) is an

analytical technique used for the elemental analysis or chemical characterization of a sample. It relies on an interaction of X-ray excitation and a sample. Its characterization capabilities are due in large part to the fundamental principle that each element has a unique atomic structure allowing unique set of peaks on its X-ray spectrum. To stimulate the emission of characteristic X-rays from a specimen, a high-energy beam of charged particles such as electrons or protons, or a beam of X-rays, is focused into the sample being studied. At rest, an atom within the sample contains ground state (or unexcited) electrons in discrete energy levels or electron shells bound to the nucleus. The incident beam may excite an electron in an inner shell, ejecting it from the shell while creating an electron hole where the electron was. An electron from an outer, higher-energy shell then fills the hole, and the difference in energy between the higher-energy shell and the lower energy shell may be released in the form of an X-ray. The number and energy of the X-rays emitted from a specimen can be measured by an energy-dispersive spectrometer. As the energy of the X-rays is characteristic of the difference in energy between the two shells, and of the atomic structure of the element from which they were emitted, this allows the elemental composition of the specimen to be measured. Figure 2.7d, e shows the two work modes of EDS, line scanning, and elemental mapping. Figure 2.7d shows the EDS line scan across a single $\text{NaYF}_4@\text{NaGdF}_4$ core@shell nanoparticle [161]. It can be seen that Y is indeed located at the center of the particle and the Gd is distributed around Y. Figure 2.7e shows the EDS elemental mapping of the $\text{NaYbF}_4:\text{Nd}@\text{Na}(\text{Yb}, \text{Gd})\text{F}_4:\text{Er}@\text{NaGdF}_4$ nanoparticles [171]. It illustrates that the elemental distributions of the nanoparticles are very consistent with the designed compositions, confirming the core@shell@shell structure of the nanoparticles.

Although the EDS can be used to analyze the chemical composition and distribution of the specimen, beam damage to nanomaterials, caused by the long scan times required for EDS, is still a challenge in the field and a limitation in some cases. Most recently, our group reported for the first time the direct imaging of the $\text{NaYF}_4:\text{Yb}, \text{Er}@\text{NaGdF}_4$ nanocrystal core@shell structure at the subnanometer on the basis of the cryo-transmission electron microscopy, rigorous EELS, and high-angle annular dark-field investigations on the core-shell structure under a low operation temperature (96 K) (Fig. 2.7f) [159].

2.5.2.2 X-ray Photoelectron Spectroscopy

X-ray photoelectron spectroscopy (XPS) is well known to be one of the most direct and effective methodologies for the determination of surface molecular and electronic structure of a material providing a good deal of information about features at the surfaces and interfaces that dominate properties of nanostructured materials. XPS easily allows a qualitative and semiquantitative analysis of the elements by measuring the binding energy (BE) of core electrons throughout the evaluation of the kinetic energy of the photoelectrons, emitted by appropriate excitation of a sample. Different oxidation states, geometries and in general chemical environments, induce BE shifts.

These features have been studied to assess the size of nanoparticles, their local structure, coatings, and interactions. XPS provides information about the actual composition, chemical state of surfaces and interfaces, and allows the evaluation of a semiquantitative concentration of the elements in the material under investigation. In fact, by evaluating the intensities and relative areas of core level signals of the elements, photoionization probability factors and photoelectrons mean free path semiquantitative data can be obtained. The sampling depth is one of the most characteristic aspects of XPS: By the imprinting X radiation with sampling depth of many hundreds Angstroms, the escape depth of the excited photoelectrons in the continuum is limited to about three times the photoelectrons mean free path, comprised between 10 and 100 Å. Therefore, this technique yields information about the outmost surface layers of the investigated materials; this is an important peculiarity when the surface plays a fundamental role, as in the case of nanostructured materials. Relative signal intensities can be useful in obtaining information about layered structures and in some cases particle sizes by using angle resolved XPS. In fact, by measuring peak intensities as a function of emission angle, it is possible to achieve information on layering, elemental enrichment, or depletion and have a detailed surface depth profile and a 3D map of the material. For example, XPS spectroscopy has been applied for the investigation of the core@shell structure of NaYF₄@NaGdF₄ nanoparticles. In the study by van Veggel et al. the XPS spectra of the core@shell NCs were measured at varying photon energies (from 250 to 1,050 eV) to determine the internal composition of the particles [89]. Experiments were performed at the Canadian Light Source, Inc. using the spherical grating monochromator (SGM) undulator beamline, 111D.1, in Saskatoon, Saskatchewan. NaYF₄@NaGdF₄ NCs in THF were deposited directly onto Au foil. After the solvent evaporated, the samples were quickly transferred to the experimental chamber. No charging effects were observed at low particle concentration. An example of a recorded XPS spectrum ($h\nu = 450$ eV), before background subtraction, is shown in Fig. 2.8a. Photoelectron spectra of elements Y³⁺ 3*d* (core) and Gd³⁺ 4*d* (shell) were recorded at increasing excitation photon energies, thus gradually increasing the sampling depth. Each spectrum was subject to a polynomial background subtraction, and the peak areas were corrected for the photoionization cross sections. The intensity ratio of Y³⁺ 3*d* to Gd³⁺ 4*d* core levels is shown in Fig. 2.8b. Changing the photon energy changes the kinetic energy range. An increase in the ratio is observed at increasing kinetic energies, demonstrating that Gd³⁺ lies predominantly on the surface of the particles. The ratio increase is caused by the screening of the Y³⁺ intensity by the surrounding Gd³⁺ atoms at low kinetic energies. Although the former characterizations, such as HAADF-STEM, EDS, etc., are all can be used to confirm the formation of the core@shell structure, XPS showed another conclusive proof for the characterization of the core@shell structure.

2.5.2.3 X-ray Diffraction

X-ray diffraction (XRD) is a tool used for identifying the atomic and molecular structure of a crystal, in which the crystalline atoms cause a beam of incident X-rays

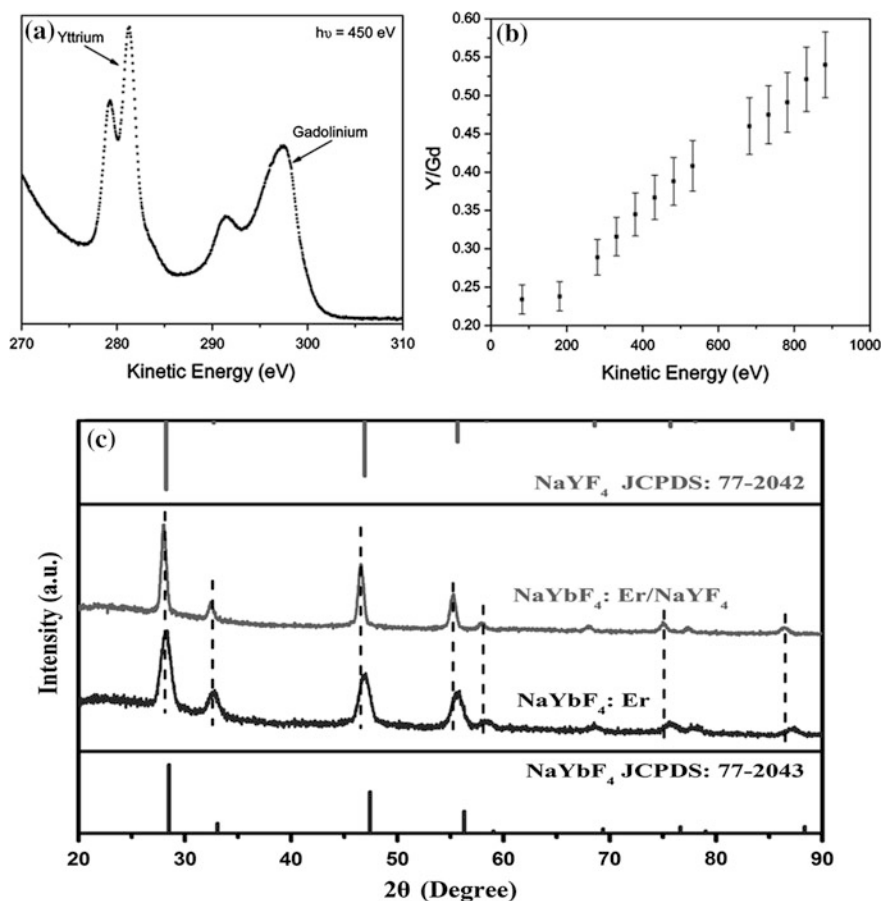


Fig. 2.8 **a** X-ray photoelectron spectroscopy of the Y³⁺ 3d and Gd³⁺ 4d core levels of NaYF₄@NaGdF₄ core@shell nanocrystals before subtraction of a polynomial background, at a photon energy of ca. 450 eV. **b** Intensity ratio of the Y³⁺ 3d to Gd³⁺ 4d core levels as a function of photoelectron kinetic energy. **c** Typical X-ray diffractions of NaYbF₄:Er and NaYbF₄:Er/NaYF₄ nanocrystals. **a**, **b** Reprinted with the permission from Ref. [89]. Copyright 2009 American Chemical Society. **c** Reprinted with the permission from Ref. [164]. Copyright 2013 American Chemical Society

to diffract into many specific directions. By measuring the angles and intensities of these diffracted beams, a crystallographer can produce a three-dimensional picture of the density of electrons within the crystal. From this electron density, the mean positions of the atoms in the crystal can be determined, as well as their chemical bonds, their disorder, and various other information. Furthermore, the XRD can also be used to evaluate the crystal size of the samples by using the Scherrer equation, which is limited to nanoscale particles and not applicable to grains larger than about 0.1–0.2 μm .

$$D = \frac{K\lambda}{B \cos \theta} \quad (2.32)$$

where D is the mean size of the crystalline domains, which may be smaller or equal to the grain size; K is a dimensionless shape factor, with a value close to unity. The shape factor has a typical value of about 0.89, but varies with the actual shape of the crystallite. λ is the X-ray wavelength, which depends on the X-ray sources. B is the line broadening at half the maximum intensity (FWHM), after subtracting the instrumental line broadening, in radians. θ is the Bragg angle, in radians. It is important to realize that the Scherrer formula provides a lower bound on the particle size. The reason for this is that a variety of factors can contribute to the width of a diffraction peak besides instrumental effects and crystallite size; the most important of these are usually inhomogeneous strain and crystal lattice imperfections. The following sources of peak broadening are as follows: dislocations, stacking faults, twinning, microstresses, grain boundaries, sub-boundaries, coherency strain, chemical heterogeneities, and crystallite smallness. (Some of those and other imperfections may also result in peak shift, peak asymmetry, anisotropic peak broadening, or affect peak shape.)

Figure 2.8c shows the typical XRD patterns of the NaYbF₄:Er core nanocrystals and corresponding NaYbF₄:Er@NaYF₄ core@shell nanocrystals [164]. It is found that both the bare core and core@shell nanocrystals exhibit a cubic crystal structure. With the growth of NaYF₄ shells, the diffraction peaks shift to lower angles consistent with the bigger lattice constant for NaYF₄, compared with NaYbF₄ crystals. In addition, the diffraction peaks become narrow gradually with the growth of NaYF₄ shells, indicating that the crystalline domain size is increased for the core/shell nanocrystals, providing direct evidence of the epitaxial growth of the shell.

2.6 Summary and Perspectives

This chapter primarily summarizes the formation mechanism of the crystallization (including nucleation and growth) for monodisperse nanocrystals, various synthetic procedures for the upconversion nanoparticles, and the optical, chemical, and structural characterizations of upconversion nanoparticles.

As aforementioned, thermolysis, Ostwald-ripening, and hydro-thermal strategies are three general approaches to produce lanthanide-doped upconversion nanoparticles. However, the quality of the same resulting upconversion nanoparticles (the same size, same shape, and same composition ratios) produced by these approaches lacks comparison, because most of the equipment used to characterize the optical properties of upconversion nanoparticles are based on the home-made instruments. Standard measurement facilities and protocols are highly required to allow the quantitative comparison of optical properties.

Although the synthetic nanochemistries described in this chapter are able to produce monodisperse upconversion nanoparticles with a diameter of 20–100 nm, it remains a challenge to produce smaller but efficient upconversion nanoparticles. The clinical translation requires that imaging agents injected into the human body should be completely cleared in a reasonable amount of time. Renal clearance is the main clearance route for imaging agents without biodegradation into biologically benign components, which requires the hydrodynamic size of nanomaterials to be smaller than 10 nm with optimized surface. Hence, developing new or modified synthetic strategies to prepare sub-10-nm upconversion nanoparticles is of crucial importance in the future. Furthermore, such an ultrasmall size of upconversion nanoparticles is always associated with a significant decrease of the luminescent efficiency due to the extremely high “surface-to-volume” ratio. Thus, nanochemistry or nanostructure dealing with ultrasmall-size-related quenching mechanisms also needs our attention.

Last but not the least, through the development of upconversion nanoparticles, the structures of the nanoparticles become increasingly advanced and ingenious. Thus, the structure, especially the core@shell structure, becomes more and more complicated, indicating that the traditional synthesis method hardly fulfills the practical needs. Therefore, the end goal is the development of the new synthesis approach which can fulfill the requirements for the fabrication of complicated multi-shell-structured upconversion nanoparticles.

References

1. Li, X., Shen, H., Niu, J., Zhang, Y., Wang, H., Li, L.S.: Columnar self-assembly of Cu_2S hexagonal nanoplates induced by Tin(IV)-X complex as inorganic surface ligand. *J. Am. Chem. Soc.* **132**, 12778–12779 (2010)
2. Li, X., Niu, J.Z., Shen, H., Xu, W., Wang, H., Li, L.S.: Shape controlled synthesis of tadpole-like and heliotrope seed-like AgInS_2 nanocrystals. *CrystEngComm* **12**, 4410–4415 (2010)
3. Li, X., Shen, H., Li, S., Niu, J.Z., Wang, H., Li, L.S.: Investigation on type-II $\text{Cu}_2\text{S-CdS}$ core/shell nanocrystals: synthesis and characterization. *J. Mater. Chem.* **20**, 923–928 (2010)
4. Li, X., Si, H., Niu, J.Z., Shen, H., Zhou, C., Yuan, H., Wang, H., Ma, L., Li, L.S.: Size-controlled syntheses and hydrophilic surface modification of Fe_3O_4 , Ag, and $\text{Fe}_3\text{O}_4/\text{Ag}$ heterodimer nanocrystals. *Dalton Trans.* **39**, 10984–10989 (2010)
5. Li, X., Wang, M., Shen, H., Zhang, Y., Wang, H., Li, L.S.: Inorganic Sn-X-complex-induced 1D, 2D, and 3D copper sulfide superstructures from anisotropic hexagonal nanoplate building blocks. *Chem. Eur. J.* **17**, 10357–10364 (2011)
6. Rogach, A.L., Talapin, D.V., Shevchenko, E.V., Kornowski, A., Haase, M., Weller, H.: Organization of matter on different size scales: monodisperse nanocrystals and their superstructures. *Adv. Funct. Mater.* **12**, 653–664 (2002)
7. Shen, H., Wang, H., Chen, X., Niu, J.Z., Xu, W., Li, X.M., Jiang, X.-D., Du, Z., Li, L.S.: Size- and shape-controlled synthesis of CdTe and PbTe nanocrystals using tellurium dioxide as the tellurium precursor. *Chem. Mater.* **22**, 4756–4761 (2010)
8. Sun, S., Ting, C.T., Wu, C.I.: The normal function of a speciation gene, *Odysseus*, and its hybrid sterility effect. *Science* **305**, 81–83 (2004)
9. Hyeon, T.: Chemical synthesis of magnetic nanoparticles. *Chem. Commun.* 927–934 (2003)

10. Park, J., Joo, J., Kwon, S.G., Jang, Y., Hyeon, T.: Synthesis of monodisperse spherical nanocrystals. *Angew. Chem. Int. Ed.* **46**, 4630–4660 (2007)
11. Bai, X., Song, H., Pan, G., Lei, Y., Wang, T., Ren, X., Lu, S., Dong, B., Dai, Q., Fan, L.: Size-dependent upconversion luminescence in $\text{Er}^{3+}/\text{Yb}^{3+}$ -codoped nanocrystalline yttria: saturation and thermal effects. *J. Phys. Chem. C* **111**, 13611–13617 (2007)
12. Mai, H.-X., Zhang, Y.-W., Sun, L.-D., Yan, C.-H.: Highly efficient multicolor up-conversion emissions and their mechanisms of monodisperse $\text{NaYF}_4:\text{Yb}$, Er core and core/shell-structured nanocrystals. *J. Phys. Chem. C* **111**, 13721–13729 (2007)
13. Chen, G., Yang, C., Prasad, P.N.: Nanophotonics and nanochemistry: controlling the excitation dynamics for frequency up- and down-conversion in lanthanide-doped nanoparticles. *Acc. Chem. Res.* **46**, 1474–1486 (2013)
14. Wang, F., Liu, X.: Upconversion multicolor fine-tuning: visible to near-infrared emission from lanthanide-doped NaYF_4 nanoparticles. *J. Am. Chem. Soc.* **130**, 5642–5643 (2008)
15. Wang, F., Chatterjee, D.K., Li, Z., Zhang, Y., Fan, X., Wang, M.: Synthesis of polyethylenimine/ NaYF_4 nanoparticles with upconversion fluorescence. *Nanotechnology* **17**, 5786–5791 (2006)
16. Li, Z., Zhang, Y.: Monodisperse silica-coated polyvinylpyrrolidone/ NaYF_4 nanocrystals with multicolor upconversion fluorescence emission. *Angew. Chem. Int. Ed.* **45**, 7732–7735 (2006)
17. Zeng, J.H., Su, J., Li, Z.H., Yan, R.X., Li, Y.D.: Synthesis and upconversion luminescence of hexagonal-phase $\text{NaYF}_4:\text{Yb}$, Er^{3+} , phosphors of controlled size and morphology. *Adv. Mater.* **17**, 2119–2123 (2005)
18. Yi, G.S., Chow, G.M.: Colloidal $\text{LaF}_3:\text{Yb}, \text{Er}$, $\text{LaF}_3:\text{Yb}, \text{Ho}$ and $\text{LaF}_3:\text{Yb}, \text{Tm}$ nanocrystals with multicolor upconversion fluorescence. *J. Mater. Chem.* **15**, 4460–4464 (2005)
19. Yi, G.S., Lu, H.C., Zhao, S.Y., Yue, G., Yang, W.J., Chen, D.P., Guo, L.H.: Synthesis, characterization, and biological application of size-controlled nanocrystalline $\text{NaYF}_4:\text{Yb}$, Er infrared-to-visible up-conversion phosphors. *Nano Lett.* **4**, 2191–2196 (2004)
20. Heer, S., Kompe, K., Gudel, H.U., Haase, M.: Highly efficient multicolour upconversion emission in transparent colloids of lanthanide-doped NaYF_4 nanocrystals. *Adv. Mater.* **16**, 2102–2105 (2004)
21. Heer, S., Lehmann, O., Haase, M., Gudel, H.U.: Blue, green, and red upconversion emission from lanthanide-doped LuPO_4 and YbPO_4 nanocrystals in a transparent colloidal solution. *Angew. Chem. Int. Ed.* **42**, 3179–3182 (2003)
22. Stouwdam, J.W., van Veggel, F.: Near-infrared emission of redispersible Er^{3+} , Nd^{3+} , and Ho^{3+} doped LaF_3 nanoparticles. *Nano Lett.* **2**, 733–737 (2002)
23. Boyer, J.-C., Cuccia, L.A., Capobianco, J.A.: Synthesis of colloidal upconverting $\text{NaYF}_4:\text{Er}^{3+}/\text{Yb}^{3+}$ and $\text{Tm}^{3+}/\text{Yb}^{3+}$ monodisperse nanocrystals. *Nano Lett.* **7**, 847–852 (2007)
24. Mai, H.X., Zhang, Y.W., Si, R., Yan, Z.G., Sun, L.D., You, L.P., Yan, C.H.: High-quality sodium rare-earth fluoride nanocrystals: controlled synthesis and optical properties. *J. Am. Chem. Soc.* **128**, 6426–6436 (2006)
25. Boyer, J.C., Vetrone, F., Cuccia, L.A., Capobianco, J.A.: Synthesis of colloidal upconverting NaYF_4 nanocrystals doped with Er^{3+} , Yb^{3+} and Tm^{3+} , Yb^{3+} via thermal decomposition of lanthanide trifluoroacetate precursors. *J. Am. Chem. Soc.* **128**, 7444–7445 (2006)
26. Zhang, Y.W., Sun, X., Si, R., You, L.P., Yan, C.H.: Single-crystalline and monodisperse LaF_3 triangular nanoplates from a single-source precursor. *J. Am. Chem. Soc.* **127**, 3260–3261 (2005)
27. Si, R., Zhang, Y.W., You, L.P., Yan, C.H.: Rare-earth oxide nanopolyhedra, nanoplates, and nanodisks. *Angew. Chem. Int. Ed.* **44**, 3256–3260 (2005)
28. Wang, L., Li, P., Li, Y.: Down- and up-conversion luminescent nanorods. *Adv. Mater.* **19**, 3304–3307 (2007)
29. Zhang, F., Zhao, D.: Synthesis of uniform rare earth fluoride (NaMF_4) nanotubes by in situ ion exchange from their hydroxide $[\text{M}(\text{OH})_3]$ parents. *ACS Nano* **3**, 159–164 (2009)

30. Zhang, F., Li, J., Shan, J., Xu, L., Zhao, D.: Shape, size, and phase-controlled rare-earth fluoride nanocrystals with optical up-conversion properties. *Chem. Eur. J.* **15**, 11010–11019 (2009)
31. Wang, G., Peng, Q., Li, Y.: Upconversion luminescence of monodisperse $\text{CaF}_2\text{:Yb}^{3+}/\text{Er}^{3+}$ nanocrystals. *J. Am. Chem. Soc.* **131**, 14200–14201 (2009)
32. Schaefer, H., Ptacek, P., Eickmeier, H., Haase, M.: Synthesis of hexagonal Yb^{3+} , Er^{3+} -doped NaYF_4 nanocrystals at low temperature. *Adv. Funct. Mater.* **19**, 3091–3097 (2009)
33. Li, Z., Zhang, Y.: An efficient and user-friendly method for the synthesis of hexagonal-phase $\text{NaYF}_4\text{:Yb}$, Er/Tm nanocrystals with controllable shape and upconversion fluorescence. *Nanotechnology* **19**, 345606 (2008)
34. Zhang, F., Wan, Y., Yu, T., Zhang, F., Shi, Y., Xie, S., Li, Y., Xu, L., Tu, B., Zhao, D.: Uniform nanostructured arrays of sodium rare-earth fluorides for highly efficient multicolor upconversion luminescence. *Angew. Chem. Int. Ed.* **46**, 7976–7979 (2007)
35. Wang, L., Li, Y.: Controlled synthesis and luminescence of lanthanide doped NaYF_4 nanocrystals. *Chem. Mater.* **19**, 727–734 (2007)
36. Wang, L., Li, Y.: $\text{Na}(\text{Y}_{1.5}\text{Na}_{0.5})\text{F}_6$ single-crystal nanorods as multicolor luminescent materials. *Nano Lett.* **6**, 1645–1649 (2006)
37. Wang, X., Zhuang, J., Peng, Q., Li, Y.D.: A general strategy for nanocrystal synthesis. *Nature* **437**, 121–124 (2005)
38. Venkatramu, V., Falcomer, D., Speghini, A., Bettinelli, M., Jayasankar, C.K.: Synthesis and luminescence properties of Er^{3+} -doped $\text{Lu}_3\text{Ga}_5\text{O}_{12}$ nanocrystals. *J. Lumin.* **128**, 811–813 (2008)
39. Yang, K., Zheng, F., Wu, R., Li, H., Zhang, X.: Upconversion luminescent properties of $\text{YVO}_4\text{:Yb}^{3+}$, Er^{3+} nano-powder by sol-gel method. *J. Rare Earths* **24**, 162–166 (2006)
40. Patra, A., Friend, C.S., Kapoor, R., Prasad, P.N.: Fluorescence upconversion properties of Er^{3+} -doped TiO_2 and BaTiO_3 nanocrystallites. *Chem. Mater.* **15**, 3650–3655 (2003)
41. Patra, A., Friend, C.S., Kapoor, R., Prasad, P.N.: Upconversion in $\text{Er}^{3+}\text{:ZrO}_2$ nanocrystals. *J. Phys. Chem. B* **106**, 1909–1912 (2002)
42. Qin, X., Yokomori, T., Ju, Y.: Flame synthesis and characterization of rare-earth (Er^{3+} , Ho^{3+} , and Tm^{3+}) doped upconversion nanophosphors. *Appl. Phys. Lett.* **90**(7), 073104 (2007)
43. Li, X., Zhang, F., Zhao, D.: Lab on upconversion nanoparticles: optical properties and applications engineering via designed nanostructure. *Chem. Soc. Rev.* doi:[10.1039/C4CS00163J](https://doi.org/10.1039/C4CS00163J) (2014)
44. Li, X., Zhang, F., Zhao, D.: Highly efficient lanthanide upconverting nanomaterials: progresses and challenges. *Nano Today* **8**, 643–676 (2013)
45. Wang, G., Peng, Q., Li, Y.: Lanthanide-doped nanocrystals: synthesis, optical-magnetic properties, and applications. *Acc. Chem. Res.* **44**, 322–332 (2011)
46. Haase, M., Schäfer, H.: Upconverting nanoparticles. *Angew. Chem. Int. Ed.* **50**, 5808–5829 (2011)
47. Wang, F., Liu, X.: Recent advances in the chemistry of lanthanide-doped upconversion nanocrystals. *Chem. Soc. Rev.* **38**, 976–989 (2009)
48. Zhou, J., Liu, Z., Li, F.: Upconversion nanophosphors for small-animal imaging. *Chem. Soc. Rev.* **41**, 1323–1349 (2012)
49. Mader, H.S., Kele, P., Saleh, S.M., Wolfbeis, O.S.: Upconverting luminescent nanoparticles for use in bioconjugation and bioimaging. *Curr. Opin. Chem. Biol.* **14**, 582–596 (2010)
50. Cheng, L., Wang, C., Liu, Z.: Upconversion nanoparticles and their composite nanostructures for biomedical imaging and cancer therapy. *Nanoscale* **5**, 23–27 (2013)
51. Chatterjee, D.K., Gnanasamandhan, M.K., Zhang, Y.: Small upconverting fluorescent nanoparticles for biomedical applications. *Small* **6**, 2781–2795 (2010)
52. Auzel, F.: Upconversion and anti-stokes processes with f and d ions in solids. *Chem. Rev.* **104**, 139–173 (2004)
53. Fischer, L.H., Harms, G.S., Wolfbeis, O.S.: Upconverting nanoparticles for nanoscale thermometry. *Angew. Chem. Int. Ed.* **50**, 4546–4551 (2011)

54. Chen, G., Qiu, H., Prasad, P.N., Chen, X.: Upconversion nanoparticles: design, nanochemistry, and applications in theranostics. *Chem. Rev.* **114**, 5161–5214 (2014)
55. Sun, X., Zhang, Y.-W., Du, Y.-P., Yan, Z.-G., Si, R., You, L.-P., Yan, C.-H.: From trifluoroacetate complex precursors to monodisperse rare-earth fluoride and oxyfluoride nanocrystals with diverse shapes through controlled fluorination in solution phase. *Chem. Eur. J.* **13**, 2320–2332 (2007)
56. Johnson, N.J.J., Korinek, A., Dong, C., van Veggel, F.C.J.M.: Self-focusing by Ostwald ripening: a strategy for layer-by-layer epitaxial growth on upconverting nanocrystals. *J. Am. Chem. Soc.* **134**, 11068–11071 (2012)
57. Li, Z., Zhang, Y., Jiang, S.: Multicolor core/shell-structured upconversion fluorescent nanoparticles. *Adv. Mater.* **20**, 4765–4769 (2008)
58. Qian, H.-S., Zhang, Y.: Synthesis of hexagonal-phase core-shell NaYF₄ nanocrystals with tunable upconversion fluorescence. *Langmuir* **24**, 12123–12125 (2008)
59. Zheng, W., Zhou, S., Chen, Z., Hu, P., Liu, Y., Tu, D., Zhu, H., Li, R., Huang, M., Chen, X.: Sub-10 nm lanthanide-doped CaF₂ nanoprobe for time-resolved luminescent biodetection. *Angew. Chem. Int. Ed.* **52**, 6671–6676 (2013)
60. Lamer, V.K., Dinegar, R.H.: Theory, production and mechanism of formation of monodispersed hydrosols. *J. Am. Chem. Soc.* **72**, 4847–4854 (1950)
61. Murray, C.B., Kagan, C., Bawendi, M.: Synthesis and characterization of monodisperse nanocrystals and close-packed nanocrystal assemblies. *Annu. Rev. Mater. Sci.* **30**, 545–610 (2000)
62. Peng, Z.A., Peng, X.G.: Nearly monodisperse and shape-controlled CdSe nanocrystals via alternative routes: nucleation and growth. *J. Am. Chem. Soc.* **124**, 3343–3353 (2002)
63. Peng, X.G., Wickham, J., Alivisatos, A.P.: Kinetics of II-VI and III-V colloidal semiconductor nanocrystal growth: “focusing” of size distributions. *J. Am. Chem. Soc.* **120**, 5343–5344 (1998)
64. Vossmeier, T., Katsikas, L., Giersig, M., Popovic, I.G., Diesner, K., Chemseddine, A., Eychmüller, A., Weller, H.: CdS nanoclusters: synthesis, characterization, size dependent oscillator strength, temperature shift of the excitonic transition energy, and reversible absorbance shift. *J. Phys. Chem.* **98**, 7665–7673 (1994)
65. Spanhel, L., Anderson, M.A.: Semiconductor clusters in the sol-gel process: quantized aggregation, gelation, and crystal growth in concentrated zinc oxide colloids. *J. Am. Chem. Soc.* **113**, 2826–2833 (1991)
66. Alivisatos, A.P.: Perspectives on the physical chemistry of semiconductor nanocrystals. *J. Phys. Chem.* **100**, 13226–13239 (1996)
67. Zhang, H.Z., Banfield, J.F.: Understanding polymorphic phase transformation behavior during growth of nanocrystalline aggregates: insights from TiO₂. *J. Phys. Chem. B* **104**, 3481–3487 (2000)
68. Murray, C.B., Norris, D.J., Bawendi, M.G.: Synthesis and characterization of nearly monodisperse CdE (E = sulfur, selenium, tellurium) semiconductor nanocrystallites. *J. Am. Chem. Soc.* **115**, 8706–8715 (1993)
69. Jana, N.R., Gearheart, L., Murphy, C.J.: Evidence for seed-mediated nucleation in the chemical reduction of gold salts to gold nanoparticles. *Chem. Mater.* **13**, 2313–2322 (2001)
70. Yu, H., Gibbons, P.C., Kelton, K.F., Buhro, W.E.: Heterogeneous seeded growth: a potentially general synthesis of monodisperse metallic nanoparticles. *J. Am. Chem. Soc.* **123**, 9198–9199 (2001)
71. Wilcoxon, J.P., Provencio, P.P.: Heterogeneous growth of metal clusters from solutions of seed nanoparticles. *J. Am. Chem. Soc.* **126**, 6402–6408 (2004)
72. Park, J., Lee, E., Hwang, N.M., Kang, M.S., Kim, S.C., Hwang, Y., Park, J.G., Noh, H.J., Kini, J.Y., Park, J.H., Hyeon, T.: One-nanometer-scale size-controlled synthesis of monodisperse magnetic iron oxide nanoparticles. *Angew. Chem. Int. Ed.* **44**, 2872–2877 (2005)

73. Talapin, D.V., Rogach, A.L., Kornowski, A., Haase, M., Weller, H.: Highly luminescent monodisperse CdSe and CdSe/ZnS nanocrystals synthesized in a hexadecylamine-trioctylphosphine oxide-trioctylphosphine mixture. *Nano Lett.* **1**, 207–211 (2001)
74. Hambrock, J., Becker, R., Birkner, A., Weiss, J., Fischer, R.A.: A non-aqueous organometallic route to highly monodispersed copper nanoparticles using [Cu(OCH(Me)CH₂NMe₂)₂]. *Chem. Commun.* 68–69 (2002)
75. Jana, N.R., Peng, X.G.: Single-phase and gram-scale routes toward nearly monodisperse Au and other noble metal nanocrystals. *J. Am. Chem. Soc.* **125**, 14280–14281 (2003)
76. Park, J., An, K.J., Hwang, Y.S., Park, J.G., Noh, H.J., Kim, J.Y., Park, J.H., Hwang, N.M., Hyeon, T.: Ultra-large-scale syntheses of monodisperse nanocrystals. *Nat. Mater.* **3**, 891–895 (2004)
77. Seo, W.S., Jo, H.H., Lee, K., Park, J.T.: Preparation and optical properties of highly crystalline, colloidal, and size-controlled indium oxide nanoparticles. *Adv. Mater.* **15**, 795–797 (2003)
78. Yu, W.W., Falkner, J.C., Yavuz, C.T., Colvin, V.L.: Synthesis of monodisperse iron oxide nanocrystals by thermal decomposition of iron carboxylate salts. *Chem. Commun.* 2306–2307 (2004)
79. Joo, J., Na, H.B., Yu, T., Yu, J.H., Kim, Y.W., Wu, F.X., Zhang, J.Z., Hyeon, T.: Generalized and facile synthesis of semiconducting metal sulfide nanocrystals. *J. Am. Chem. Soc.* **125**, 11100–11105 (2003)
80. Yi, G.-S., Chow, G.-M.: Water-soluble NaYF₄:Yb, Er(Tm)/NaYF₄/polymer core/shell/shell nanoparticles with significant enhancement of upconversion fluorescence. *Chem. Mater.* **19**, 341–434 (2007)
81. Reiss, H.: The growth of uniform colloidal dispersions. *J. Chem. Phys.* **19**, 482–487 (1951)
82. Talapin, D.V., Rogach, A.L., Haase, M., Weller, H.: Evolution of an ensemble of nanoparticles in a colloidal solution: theoretical study. *J. Phys. Chem. B* **105**, 12278–12285 (2001)
83. Talapin, D.V., Rogach, A.L., Shevchenko, E.V., Kornowski, A., Haase, M., Weller, H.: Dynamic distribution of growth rates within the ensembles of colloidal II–VI and III–V semiconductor nanocrystals as a factor governing their photoluminescence efficiency. *J. Am. Chem. Soc.* **124**, 5782–5790 (2002)
84. Chen, G., Shen, J., Ohulchanskyy, T.Y., Patel, N.J., Kutikov, A., Li, Z., Song, J., Pandey, R. K., Agren, H., Prasad, P.N., Han, G.: (α-NaYbF₄:Tm³⁺)/CaF₂ core/shell nanoparticles with efficient near-infrared to near-infrared upconversion for high-contrast deep tissue bioimaging. *ACS Nano* **6**, 8280–8287 (2012)
85. Zhan, Q., Qian, J., Liang, H., Somesfalean, G., Wang, D., He, S., Zhang, Z., Andersson-Engels, S.: Using 915 nm laser excited Tm³⁺/Er³⁺/Ho³⁺-doped NaYbF₄ upconversion nanoparticles for in vitro and deeper in vivo bioimaging without overheating irradiation. *ACS Nano* **5**, 3744–3757 (2011)
86. Chen, G., Ohulchanskyy, T.Y., Liu, S., Law, W.-C., Wu, F., Swihart, M.T., Agren, H., Prasad, P.N.: Core/shell NaGdF₄:Nd³⁺/NaGdF₄ nanocrystals with efficient near-infrared to near-infrared downconversion photoluminescence for bioimaging applications. *ACS Nano* **6**, 2969–2977 (2012)
87. Vetrone, F., Naccache, R., Mahalingam, V., Morgan, C.G., Capobianco, J.A.: The active-core/active-shell approach: a strategy to enhance the upconversion luminescence in lanthanide-doped nanoparticles. *Adv. Funct. Mater.* **19**, 2924–2929 (2009)
88. Naccache, R., Vetrone, F., Mahalingam, V., Cuccia, L.A., Capobianco, J.A.: Controlled synthesis and water dispersibility of hexagonal phase NaGdF₄:Ho³⁺/Yb³⁺ nanoparticles. *Chem. Mater.* **21**, 717–723 (2009)
89. Abel, K.A., Boyer, J.-C., van Veggel, F.C.J.M.: Hard proof of the NaYF₄/NaGdF₄ nanocrystal core/shell structure. *J. Am. Chem. Soc.* **131**, 14644–14645 (2009)
90. Ye, X., Collins, J.E., Kang, Y., Chen, J., Chen, D.T.N., Yodh, A.G., Murray, C.B.: Morphologically controlled synthesis of colloidal upconversion nanophosphors and their shape-directed self-assembly. *Proc. Natl. Acad. Sci.* **107**, 22430–22435 (2010)

91. Kombar, R., Klare, J.P., Voss, B., Nordmann, J., Steinhoff, H.-J., Haase, M.: An electron paramagnetic resonance spectroscopic investigation on the growth mechanism of $\text{NaYF}_4\text{:Gd}$ nanocrystals. *Angew. Chem. Int. Ed.* **51**, 6506–6510 (2012)
92. Mahalingam, V., Vetrone, F., Naccache, R., Speghini, A., Capobianco, J.A.: Colloidal $\text{Tm}^{3+}/\text{Yb}^{3+}$ -doped LiYF_4 nanocrystals: multiple luminescence spanning the UV to NIR regions via low-energy excitation. *Adv. Mater.* **21**, 4025–4028 (2009)
93. Wang, J., Wang, F., Xu, J., Wang, Y., Liu, Y., Chen, X., Chen, H., Liu, X.: Lanthanide-doped LiYF_4 nanoparticles: synthesis and multicolor upconversion tuning. *C. R. Chim.* **13**, 731–736 (2010)
94. Chen, G., Ohulchanskyy, T.Y., Kachynski, A., Agren, H., Prasad, P.N.: Intense visible and near-infrared upconversion photoluminescence in colloidal $\text{LiYF}_4\text{:Er}^{3+}$ nanocrystals under excitation at 1490 nm. *ACS Nano* **5**, 4981–4986 (2011)
95. Zhou, H.-P., Zhang, Y.-W., Mai, H.-X., Sun, X., Liu, Q., Song, W.-G., Yan, C.-H.: Spontaneous organization of uniform CeO_2 nanoflowers by 3D oriented attachment in hot surfactant solutions monitored with an in situ electrical conductance technique. *Chem. Eur. J.* **14**, 3380–3390 (2008)
96. Qiu, H., Chen, G., Fan, R., Cheng, C., Hao, S., Chen, D., Yang, C.: Tuning the size and shape of colloidal cerium oxide nanocrystals through lanthanide doping. *Chem. Commun.* **47**, 9648–9650 (2011)
97. Chen, G., Qiu, H., Fan, R., Hao, S., Tan, S., Yang, C., Han, G.: Lanthanide-doped ultrasmall yttrium fluoride nanoparticles with enhanced multicolor upconversion photoluminescence. *J. Mater. Chem.* **22**, 20190–20196 (2012)
98. Du, Y.P., Sun, X., Zhang, Y.W., Yan, Z.G., Sun, L.D., Yan, C.H.: Uniform alkaline earth fluoride nanocrystals with diverse shapes grown from thermolysis of metal trifluoroacetates in hot surfactant solutions. *Cryst. Growth Des.* **9**, 2013–2019 (2009)
99. Teng, X., Zhu, Y., Wei, W., Wang, S., Huang, J., Naccache, R., Hu, W., Tok, A.I.Y., Han, Y., Zhang, Q., Fan, Q., Huang, W., Capobianco, J.A., Huang, L.: Lanthanide-doped $\text{Na}_x\text{ScF}_{3+x}$ nanocrystals: crystal structure evolution and multicolor tuning. *J. Am. Chem. Soc.* **134**, 8340–8343 (2012)
100. Yi, G.S., Chow, G.M.: Synthesis of hexagonal-phase $\text{NaYF}_4\text{:Yb}$, Er and $\text{NaYF}_4\text{:Yb}$, Tm nanocrystals with efficient up-conversion fluorescence. *Adv. Funct. Mater.* **16**, 2324–2329 (2006)
101. Du, Y.-P., Zhang, Y.-W., Sun, L.-D., Yan, C.-H.: Luminescent monodisperse nanocrystals of lanthanide oxyfluorides synthesized from trifluoroacetate precursors in high-boiling solvents. *J. Phys. Chem. C* **112**, 405–415 (2008)
102. Du, Y.-P., Zhang, Y.-W., Sun, L.-D., Yan, C.-H.: Atomically efficient synthesis of self-assembled monodisperse and ultrathin lanthanide oxychloride nanoplates. *J. Am. Chem. Soc.* **131**, 3162–3163 (2009)
103. Niu, W., Wu, S., Zhang, S.: Utilizing the amidation reaction to address the “cooperative effect” of carboxylic acid/amine on the size, shape, and multicolor output of fluoride upconversion nanoparticles. *J. Mater. Chem.* **21**, 10894–10902 (2011)
104. Chen, G., Ohulchanskyy, T.Y., Kumar, R., Agren, H., Prasad, P.N.: Ultrasmall monodisperse $\text{NaYF}_4\text{:Yb}^{3+}/\text{Tm}^{3+}$ nanocrystals with enhanced near-infrared to near-infrared upconversion photoluminescence. *ACS Nano* **4**, 3163–3168 (2010)
105. Si, R., Zhang, Y.-W., Zhou, H.-P., Sun, L.-D., Yan, C.-H.: Controlled-synthesis, self-assembly behavior, and surface-dependent optical properties of high-quality rare-earth oxide nanocrystals. *Chem. Mater.* **19**, 18–27 (2007)
106. Cao, Y.C.: Synthesis of square gadolinium-oxide nanoplates. *J. Am. Chem. Soc.* **126**, 7456–7457 (2004)
107. Zhao, F., Yuan, M., Zhang, W., Gao, S.: Monodisperse lanthanide oxysulfide nanocrystals. *J. Am. Chem. Soc.* **128**, 11758–11759 (2006)
108. Ding, Y., Gu, J., Ke, J., Zhang, Y.-W., Yan, C.-H.: Sodium doping controlled synthesis of monodisperse lanthanide oxysulfide ultrathin nanoplates guided by density functional calculations. *Angew. Chem. Int. Ed.* **50**, 12330–12334 (2011)

109. Ding, Y., Gu, J., Zhang, T., Yin, A.-X., Yang, L., Zhang, Y.-W., Yan, C.-H.: Chemoaffinity-mediated synthesis of NaRES₂-based nanocrystals as versatile nano-building blocks and durable nano-pigments. *J. Am. Chem. Soc.* **134**, 3255–3264 (2012)
110. Wang, F., Sun, L.-D., Gu, J., Wang, Y.-F., Feng, W., Yang, Y., Wang, J., Yan, C.-H.: Selective heteroepitaxial nanocrystal growth of rare earth fluorides on sodium chloride: synthesis and density functional calculations. *Angew. Chem. Int. Ed.* **51**, 8796–8799 (2012)
111. Zhou, H.-P., Zhang, C., Yan, C.-H.: Controllable assembly of diverse rare-earth nanocrystals via the langmuir-blodgett technique and the underlying size- and symmetry-dependent assembly kinetics. *Langmuir* **25**, 12914–12925 (2009)
112. Wang, H.Z., Uehara, M., Nakamura, H., Miyazaki, M., Maeda, H.: Synthesis of well-dispersed Y₂O₃:Eu nanocrystals and self-assembled nanodisks using a simple non-hydrolytic route. *Adv. Mater.* **17**, 2506–2509 (2005)
113. Shan, J., Qin, X., Yao, N., Ju, Y.: Synthesis of monodisperse hexagonal NaYF₄: Yb, Ln (Ln = Er, Ho and Tm) upconversion nanocrystals in TOPO. *Nanotechnology* **18** (2007)
114. Shan, J., Kong, W., Wei, R., Yao, N., Ju, Y.: An investigation of the thermal sensitivity and stability of the beta-NaYF₄:Yb, Er upconversion nanophosphors. *J. Appl. Phys.* **107** (2010)
115. Shan, J., Ju, Y.: Controlled synthesis of lanthanide-doped NaYF₄ upconversion nanocrystals via ligand induced crystal phase transition and silica coating. *Appl. Phys. Lett.* **91** (2007)
116. He, M., Huang, P., Zhang, C., Chen, F., Wang, C., Ma, J., He, R., Cui, D.: A general strategy for the synthesis of upconversion rare earth fluoride nanocrystals via a novel OA/ionic liquid two-phase system. *Chem. Commun.* **47**, 9510–9512 (2011)
117. Li, P., Peng, Q., Li, Y.: Dual-mode luminescent colloidal spheres from monodisperse rare-earth fluoride nanocrystals. *Adv. Mater.* **21**, 1945–1948 (2009)
118. Chen, D., Huang, P., Yu, Y., Huang, F., Yang, A., Wang, Y.: Dopant-induced phase transition: a new strategy of synthesizing hexagonal upconversion NaYF₄ at low temperature. *Chem. Commun.* **47**, 5801–5803 (2011)
119. Chen, Z., Chen, H., Hu, H., Yu, M., Li, F., Zhang, Q., Zhou, Z., Yi, T., Huang, C.: Versatile synthesis strategy for carboxylic acid-functionalized upconverting nanophosphors as biological labels. *J. Am. Chem. Soc.* **130**, 3023–3029 (2008)
120. Nguyen, T.-D., Dinh, C.-T., Do, T.-O.: Shape- and size-controlled synthesis of monoclinic ErOOH and cubic Er₂O₃ from micro- to nanostructures and their upconversion luminescence. *ACS Nano* **4**, 2263–2273 (2010)
121. Qiu, H., Chen, G., Sun, L., Hao, S., Han, G., Yang, C.: Ethylenediaminetetraacetic acid (EDTA)-controlled synthesis of multicolor lanthanide doped BaYF₅ upconversion nanocrystals. *J. Mater. Chem.* **21**, 17202–17208 (2011)
122. Yang, S., Gao, L.: Controlled synthesis and self-assembly of CeO₂ nanocubes. *J. Am. Chem. Soc.* **128**, 9330–9331 (2006)
123. Chen, D., Yu, Y., Huang, F., Huang, P., Yang, A., Wang, Y.: Modifying the size and shape of monodisperse bifunctional alkaline-earth fluoride nanocrystals through lanthanide doping. *J. Am. Chem. Soc.* **132**, 9976–9978 (2010)
124. Zhu, X., Zhang, Q., Li, Y., Wang, H.: Redispersible and water-soluble LaF₃:Ce, Tb nanocrystals via a microfluidic reactor with temperature steps. *J. Mater. Chem.* **18**, 5060–5062 (2008)
125. Li, S., Xie, T., Peng, Q., Li, Y.: Nucleation and growth of CeF₃ and NaCeF₄ nanocrystals. *Chem. Eur. J.* **15**, 2512–2517 (2009)
126. Chen, D., Yu, Y., Huang, F., Wang, Y.: Phase transition from hexagonal LnF₃ (Ln = La, Ce, Pr) to cubic Ln_{0.8}M_{0.2}F_{2.8} (M = Ca, Sr, Ba) nanocrystals with enhanced upconversion induced by alkaline-earth doping. *Chem. Commun.* **47**, 2601–2603 (2011)
127. Chen, D., Lei, L., Zhang, R., Yang, A., Xu, J., Wang, Y.: Intrinsic single-band upconversion emission in colloidal Yb/Er(Tm):Na₃Zr(Hf)F₇ nanocrystals. *Chem. Commun.* **48**, 10630–10632 (2012)
128. Wang, G., Peng, Q., Li, Y.: Synthesis and upconversion luminescence of BaY₂F₈:Yb³⁺/Er³⁺ nanobelts. *Chem. Commun.* **46**, 7528–7529 (2010)

129. Schaefer, H., Ptacek, P., Zerzouf, O., Haase, M.: Synthesis and optical properties of KYF₄/Yb, Er nanocrystals, and their surface modification with undoped KYF₄. *Adv. Funct. Mater.* **18**, 2913–2918 (2008)
130. Shi, F., Wang, J., Zhai, X., Zhao, D., Qin, W.: Facile synthesis of beta-NaLuF₄:Yb/Tm hexagonal nanoplates with intense ultraviolet upconversion luminescence. *CrystEngComm* **13**, 3782–3787 (2011)
131. Peng, Y., Xing, M.-M., Luo, X.-X., Wang, L.-Q.: Synthesis and characteristic research of nanoparticles KY₃F₁₀:Yb, RE (RE = Er, Ho, Tm) by thermal decomposition. *Acta Phys. Sin-Ch. Ed.* **61** (2012)
132. Vetrone, F., Mahalingam, V., Capobianco, J.A.: Near-infrared-to-blue upconversion in colloidal BaYF₅:Tm³⁺, Yb³⁺ nanocrystals. *Chem. Mater.* **21**, 1847–1851 (2009)
133. Wang, Y.-F., Sun, L.-D., Xiao, J.-W., Feng, W., Zhou, J.-C., Shen, J., Yan, C.-H.: Rare-earth nanoparticles with enhanced upconversion emission and suppressed rare-earth-ion leakage. *Chem. Eur. J.* **18**, 5558–5564 (2012)
134. Byrappa, K., Adschiri, T.: Hydrothermal technology for nanotechnology. *Prog. Cryst. Growth Ch* **53**, 117–166 (2007)
135. Haes, A.J., Van Duyne, R.P.: A nanoscale optical biosensor: sensitivity and selectivity of an approach based on the localized surface plasmon resonance spectroscopy of triangular silver nanoparticles. *J. Am. Chem. Soc.* **124**, 10596–10604 (2002)
136. Wang, L., Qin, W., Liu, Z., Zhao, D., Qin, G., Di, W., He, C.: Improved 800 nm emission of Tm³⁺ sensitized by Yb³⁺ and Ho³⁺ in beta-NaYF₄ nanocrystals under 980 nm excitation. *Opt. Express* **20**, 7602–7607 (2012)
137. Jiang, W., Kim, B.Y.S., Rutka, J.T., Chan, W.C.W.: Nanoparticle-mediated cellular response is size-dependent. *Nat. Nanotechnol.* **3**, 145–150 (2008)
138. Shaner, N.C., Steinbach, P.A., Tsien, R.Y.: A guide to choosing fluorescent proteins. *Nat. Methods* **2**, 905–909 (2005)
139. Yang, D., Kang, X., Shang, M., Li, G., Peng, C., Li, C., Lin, J.: Size and shape controllable synthesis and luminescent properties of BaGdF₅: Ce³⁺/Ln³⁺ (Ln = Sm, Dy, Eu, Tb) nano/submicrocrystals by a facile hydrothermal process. *Nanoscale* **3**, 2589–2595 (2011)
140. Liu, Z.-J., Song, X.-X., Tang, Q.: Development of PEGylated KMnF₃ nanoparticles as a T-1-weighted contrast agent: chemical synthesis, in vivo brain MR imaging, and accounting for high relaxivity. *Nanoscale* **5**, 5073–5079 (2013)
141. Yan, R.X., Li, Y.D.: Down/up conversion in Ln³⁺-doped YF₃ nanocrystals. *Adv. Funct. Mater.* **15**, 763–770 (2005)
142. Lemyre, J.L., Ritcey, A.M.: Synthesis of lanthanide fluoride nanoparticles of varying shape and size. *Chem. Mater.* **17**, 3040–3043 (2005)
143. Li, C., Yang, J., Yang, P., Lian, H., Lin, J.: Hydrothermal synthesis of lanthanide fluorides LnF₃ (Ln = La to Lu) nano-/microcrystals with multiform structures and morphologies. *Chem. Mater.* **20**, 4317–4326 (2008)
144. Fu, Z., Zheng, H., He, E., Gao, W., Li, G.: Enhancement of red emission by co-dopant Ln³⁺ ions in Eu³⁺:LaOF nanoparticles. *Sci. China Phys. Mech. Astron.* **56**, 928–932 (2013)
145. Wang, F., Han, Y., Lim, C.S., Lu, Y., Wang, J., Xu, J., Chen, H., Zhang, C., Hong, M., Liu, X.: Simultaneous phase and size control of upconversion nanocrystals through lanthanide doping. *Nature* **463**, 1061–1065 (2010)
146. Liu, Q., Sun, Y., Yang, T., Feng, W., Li, C., Li, F.: Sub-10 nm hexagonal lanthanide-doped NaLuF₄ upconversion nanocrystals for sensitive bioimaging in vivo. *J. Am. Chem. Soc.* **133**, 17122–17125 (2011)
147. Li, C., Quan, Z., Yang, P., Yang, J., Lian, H., Lin, J.: Shape controllable synthesis and upconversion properties of NaYbF₄/NaYbF₄:Er³⁺ and YbF₃/YbF₃:Er³⁺ microstructures. *J. Mater. Chem.* **18**, 1353–1361 (2008)
148. Ostrowski, A.D., Chan, E.M., Gargas, D.J., Katz, E.M., Han, G., Schuck, P.J., Milliron, D.J., Cohen, B.E.: Controlled synthesis and single-particle imaging of bright, sub-10 nm lanthanide-doped upconverting nanocrystals. *ACS Nano* **6**, 2686–2692 (2012)

149. Johnson, N.J.J., Oakden, W., Stanisiz, G.J., Prosser, R.S., van Veggel, F.C.J.M.: Size-tunable, ultrasmall NaGdF₄ nanoparticles: insights into their T1 MRI contrast enhancement. *Chem. Mater.* **23**, 3714–3722 (2011)
150. Zheng, W., Zhou, S., Chen, Z., Hu, P., Liu, Y., Tu, D., Zhu, H., Li, R., Huang, M., Chen, X.: Sub-10 nm lanthanide-doped CaF₂ nanoprobes for time-resolved luminescent biodetection. *Angew. Chem. Int. Ed.* **52**, 6671–6676 (2013)
151. Chen, D., Yu, Y., Huang, F., Lin, H., Huang, P., Yang, A., Wang, Z., Wang, Y.: Lanthanide dopant-induced formation of uniform sub-10 nm active-core/active-shell nanocrystals with near-infrared to near-infrared dual-modal luminescence. *J. Mater. Chem.* **22**, 2632–2640 (2012)
152. Xu, L., Yu, Y., Li, X., Somesfalean, G., Zhang, Y., Gao, H., Zhang, Z.: Synthesis and upconversion properties of monoclinic Gd₂O₃:Er³⁺ nanocrystals. *Opt. Mater.* **30**, 1284–1288 (2008)
153. X-x, Luo, W-h, Cao: Ethanol-assistant solution combustion method to prepare La₂O₂S:Yb, Pr nanometer phosphor. *J. Alloy. Compd.* **460**, 529–534 (2008)
154. Vetrone, F., Boyer, J.C., Capobianco, J.A., Speghini, A., Bettinelli, M.: Significance of Yb³⁺ concentration on the upconversion mechanisms in codoped Y₂O₃:Er³⁺, Yb³⁺ nanocrystals. *J. Appl. Phys.* **96**, 661–667 (2004)
155. Boyer, J.-C., van Veggel, F.C.J.M.: Absolute quantum yield measurements of colloidal NaYF₄: Er³⁺, Yb³⁺ upconverting nanoparticles. *Nanoscale* **2**, 1417–1419 (2010)
156. Sarkar, S., Meesaragandla, B., Hazra, C., Mahalingam, V.: Sub-5 nm Ln³⁺-doped BaLuF₅ nanocrystals: a platform to realize upconversion via interparticle energy transfer (IPET). *Adv. Mater.* **25**, 856–860 (2013)
157. Wong, H.-T., Vetrone, F., Naccache, R., Chan, H.L.W., Hao, J., Capobianco, J.A.: Water dispersible ultra-small multifunctional KGdF₄:Tm³⁺, Yb³⁺ nanoparticles with near-infrared to near-infrared upconversion. *J. Mater. Chem.* **21**, 16589–16596 (2011)
158. Wang, F., Deng, R., Wang, J., Wang, Q., Han, Y., Zhu, H., Chen, X., Liu, X.: Tuning upconversion through energy migration in core-shell nanoparticles. *Nat. Mater.* **10**, 968–973 (2011)
159. Zhang, F., Che, R., Li, X., Yao, C., Yang, J., Shen, D., Hu, P., Li, W., Zhao, D.: Direct imaging the upconversion nanocrystal core/shell structure at the subnanometer level: shell thickness dependence in upconverting optical properties. *Nano Lett.* **12**, 2852–2858 (2012)
160. Wang, F., Wang, J., Liu, X.: Direct evidence of a surface quenching effect on size-dependent luminescence of upconversion nanoparticles. *Angew. Chem. Int. Ed.* **49**, 7456–7460 (2010)
161. Abel, K.A., Boyer, J.-C., Andrei, C.M., van Veggel, F.C.J.M.: Analysis of the shell thickness distribution on NaYF₄/NaGdF₄ core/shell nanocrystals by EELS and EDS. *J. Phys. Chem. L.* **2**, 185–189 (2011)
162. Li, X., Wang, R., Zhang, F., Zhou, L., Shen, D., Yao, C., Zhao, D.: Nd³⁺ sensitized up/down converting dual-mode nanomaterials for efficient in-vitro and in-vivo bioimaging excited at 800 nm. *Sci. Rep.* **3**, 3536 (2013)
163. Huang, P., Zheng, W., Zhou, S., Tu, D., Chen, Z., Zhu, H., Li, R., Ma, E., Huang, M., Chen, X.: Lanthanide-doped LiLuF₄ upconversion nanoprobes for the detection of disease biomarkers. *Angew. Chem. Int. Ed.* **53**, 1252–1257 (2014)
164. Li, X., Shen, D., Yang, J., Yao, C., Che, R., Zhang, F., Zhao, D.: Successive layer-by-layer strategy for multi-shell epitaxial growth: shell thickness and doping position dependence in upconverting optical properties. *Chem. Mater.* **25**, 106–112 (2013)
165. Dong, C., Korinek, A., Blasiak, B., Tomanek, B., van Veggel, F.C.J.M.: Cation exchange: a facile method to make NaYF₄:Yb, Tm-NaGdF₄ core-shell nanoparticles with a thin, tunable, and uniform shell. *Chem. Mater.* **24**, 1297–1305 (2012)
166. Li, X., Wang, R., Zhang, F., Zhao, D.: Engineering homogeneous doping in single nanoparticle to enhance upconversion efficiency. *Nano Lett.* **14**, 3634–3639 (2014)

167. Li, J.J., Wang, Y.A., Guo, W.Z., Keay, J.C., Mishima, T.D., Johnson, M.B., Peng, X.G.: Large-scale synthesis of nearly monodisperse CdSe/CdS core/shell nanocrystals using air-stable reagents via successive ion layer adsorption and reaction. *J. Am. Chem. Soc.* **125**, 12567–12575 (2003)
168. Dong, C., van Veggel, F.C.J.M.: Cation exchange in lanthanide fluoride nanoparticles. *ACS Nano* **3**, 123–130 (2009)
169. Liu, Q., Sun, Y., Li, C., Zhou, J., Li, C., Yang, T., Zhang, X., Yi, T., Wu, D., Li, F.: F-18-labeled magnetic-upconversion nanophosphors via rare-earth cation-assisted ligand assembly. *ACS Nano* **5**, 3146–3157 (2011)
170. Xu, C.T., Svenmarker, P., Liu, H., Wu, X., Messing, M.E., Wallenberg, L.R., Andersson-Engels, S.: High-resolution fluorescence diffuse optical tomography developed with nonlinear upconverting nanoparticles. *ACS Nano* **6**, 4788–4795 (2012)
171. Wen, H., Zhu, H., Chen, X., Hung, T.F., Wang, B., Zhu, G., Yu, S.F., Wang, F.: Upconverting near-infrared light through energy management in core-shell-shell nanoparticles. *Angew. Chem. Int. Ed.* **125**, 13661–13665 (2013)

Photon Upconversion Nanomaterials

Zhang, F.

2015, XIX, 416 p. 68 illus., 58 illus. in color., Hardcover

ISBN: 978-3-662-45596-8